

ARTICLE

Structural design and testing of material optimized ribbed RC slabs with 3D printed formwork

Tobias Huber^{1,2}  | Joris Burger³  | Jaime Mata-Falcón¹  |
Walter Kaufmann¹ 

¹Institute of Structural Engineering, ETH Zurich, Zurich, Switzerland

²Institute of Structural Engineering, TU Wien, Vienna, Austria

³Institute of Technology in Architecture, ETH Zurich, Zurich, Switzerland

Correspondence

Tobias Huber, Stefano-Franscini-Platz 5, 8093 Zurich, Switzerland.

Email: tobias.huber@ibk.baug.ethz.ch

Funding information

ETH Zürich Foundation; Geberit; Siemens; Swiss National Science Foundation's NCCR Digital Fabrication, Grant/Award Number: 51NF40-141853

Abstract

Most of the concrete volume in multistorey buildings is cast in solid slabs, which are frequently flat slabs supported on columns. By using two-way spanning ribbed slabs, concrete consumption could be significantly reduced. However, due to the high costs associated with formwork, such a complex rib configuration is rarely used nowadays. With the advent of technologies for automated formwork fabrication, the material-saving potential inherent in this structural system could again be exploited. This paper investigates the feasibility of material-efficient ribbed concrete slabs on a building scale using conventional concrete and steel reinforcing bars cast inside a three-dimensional-printed plastic-based formwork. To that end, the code-compliant design of ribbed slabs is first discussed, followed by the introduction of a concept for an automated design-to-production workflow. The sustainability of this slab system is compared to a solution using conventional formwork in a case study consisting of a multibay office building with slabs spanning 8 m in both directions, revealing that ribbed slabs use 40% less concrete than solid slabs. Several representative structural elements of the case study (ribs, slab-column transition) were produced at full-scale and tested until failure to investigate the feasibility of production and structural performance. Three T-beams with various rib shapes (straight, kinked with diaphragms, curved) were tested in a three-point bending configuration, showing a ductile behavior with longitudinal reinforcement yielding and indicating the relevance of torsional effects in curved ribs. Punching tests on two slab-column connections (ribbed, solid) revealed that the optimized ribbed slab could prevent brittle punching failures and achieve an ultimate load 105% higher than the solid reference slab. All specimens' load-bearing behavior could be predicted using established design formulas, showing the feasibility of producing code-compliant ribbed slabs with the applied technology.

Discussion on this paper must be submitted within two months of the print publication. The discussion will then be published in print, along with the authors' closure, if any, approximately nine months after the print publication.

This is an open access article under the terms of the [Creative Commons Attribution](https://creativecommons.org/licenses/by/4.0/) License, which permits use, distribution and reproduction in any medium, provided the original work is properly cited.

© 2023 The Authors. *Structural Concrete* published by John Wiley & Sons Ltd on behalf of International Federation for Structural Concrete.

KEYWORDS

automated formwork, digital fabrication, eggshell, optimization, prototype, punching, ribbed slabs, testing

1 | INTRODUCTION

Material-efficient ribbed slabs¹ (Figure 1a,b) and mushroom slabs^{2,3} (Figure 1c) were the state-of-the-art solutions for building floor slabs since the beginnings of reinforced concrete (RC) construction. Pier Luigi Nervi and his employee Aldo Arcangeli designed even more efficient ribbed floor slabs by aligning the ribs with the principal bending moment trajectories rather than using an orthogonal grid⁴ (Figure 1b). This concept was also followed by other designers and is sometimes referred to as biomimetic⁵ (Figure 1a). While these solutions combine appealing esthetics with optimized structural efficiency, they were abandoned due to the high amount of labor and associated costs required to build the geometrically complex formwork and reinforcement. While automated bending of reinforcing bars is commonly available

today, customized formwork production (e.g., produced manually or CNC-milled wood or polystyrene elements) is still difficult and wasteful. Because cement production is one of the major contributors to the construction sector's carbon footprint,⁶ material optimized structures are desirable on the European Union's path to climate neutrality.⁷

Modular slab systems available today make use of the potential for reducing concrete and weight by introducing voids or substituting lighter materials for concrete. Hollow-core slabs (Figure 1d) or filigree slabs (Figure 1e, e.g., with clay bricks or polymer foam blocks) are frequently used for one-way slabs. Material-efficient commercial two-way slab systems employ either void generators (Figure 1f, e.g., Cobiax[®]) or plastic mold elements (Figure 1g, e.g., Holedeck[®], Skydome[®]). All systems have some limitations in terms

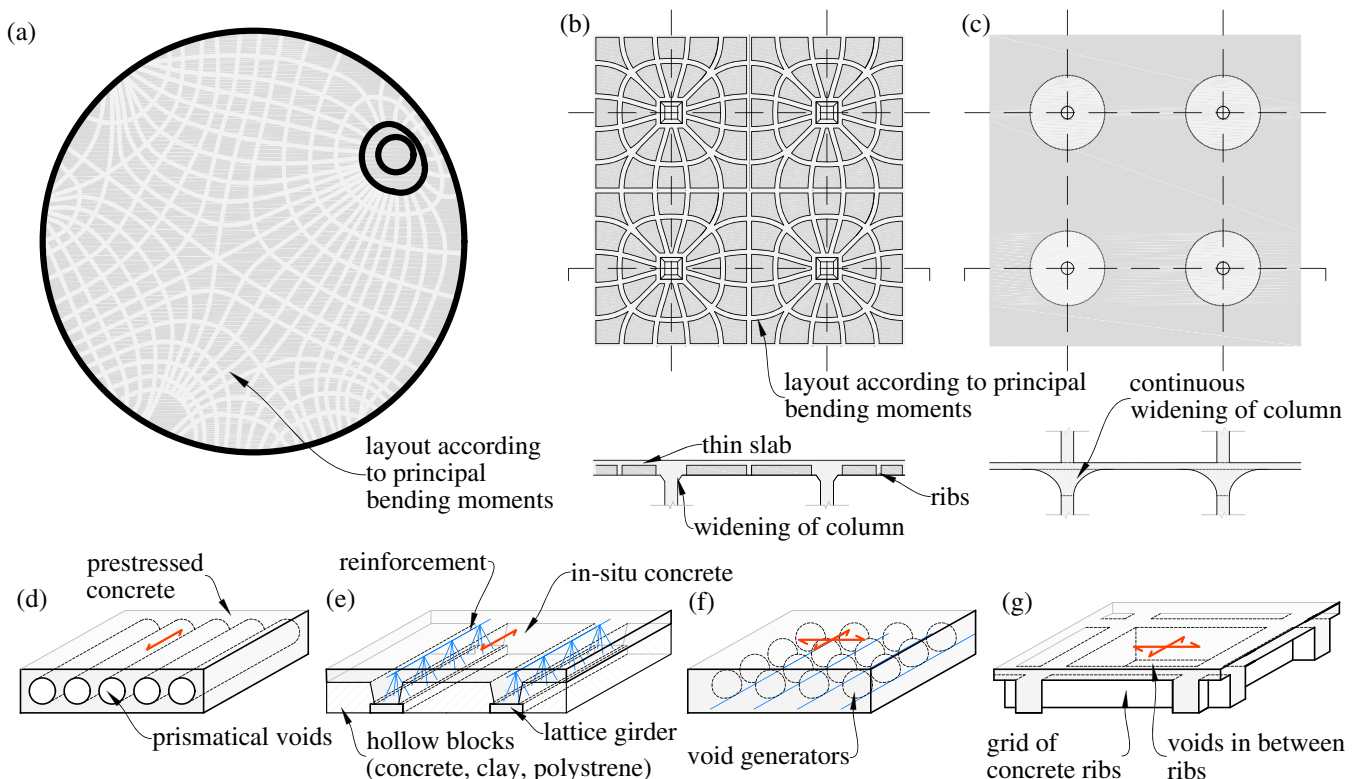


FIGURE 1 Material-efficient slabs: (a) schematic rib layout of the former zoological lecture hall at the University of Freiburg (1968) of Hans-Dieter Hecker (adapted from⁵); (b) ribbed slab inspired by Gatti wool factory (1951) of Pier Luigi Nervi (adapted from⁴); (c) mushroom slab inspired by grain warehouse in Altdorf (1912) of Robert Maillart; (d) hollow-core slabs, (e) filigree slabs, (f) slabs with void generators, and (g) waffle slabs.

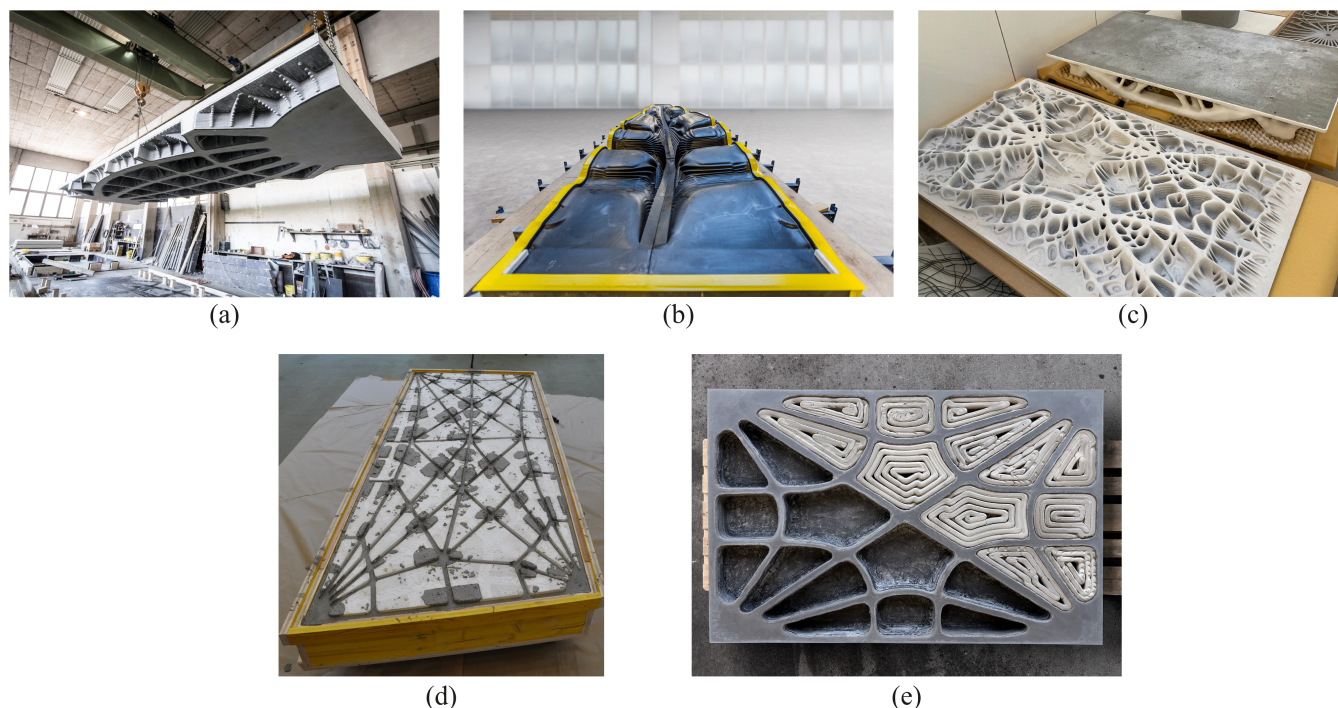


FIGURE 2 Examples of slabs built with automated formwork: (a) 3D-extrusion printing of concrete²⁴ © Robert Schmid; (b) binder jetted polyester formwork¹⁷ © Andrei Jipa; (c) binder jetted sandstone formwork²²; (d) funicular floor slab with CNC-milled polystyrene inlays¹⁸ © Andrew Liew; and (e) ribbed slab with printed mineral foam inlays²¹ © Patrick Bedarf.

of esthetics and customization. Furthermore, the use of stay-in-place polymer void elements is environmentally questionable.

Automated formwork systems (digital formworks) aim at fabricating complex formworks at competitive costs⁸ while using low amounts of material, and energy. Several studies have recently discussed the benefits and drawbacks of upcoming approaches for automated formwork production.^{9–11} Using automated formwork production for customized two-way RC ribbed slabs (see Figure 1a,b) could significantly reduce material consumption on a structural level¹², as slabs require approximately 80% of the concrete volume in typical multistorey buildings^{13,14} or approximately 55% in smaller buildings.¹⁵ Despite the importance of this structural typology, only a few studies have addressed digital fabrication of slabs^{16–24} (see Figure 2 and Table 1). These studies describe various slab prototypes using various concepts for formwork, reinforcement and concrete. Table 1 summarizes the properties of the slab prototypes described.

Several studies^{25–27} have addressed the challenge of introducing conventional reinforcement into digital fabrication processes. Accordingly, the studies described in Table 1 primarily focus on approaches that do not use conventional reinforcing bars, either by using FRC or

UHPFRC^{18,20–22} or by relying on post-tensioning,^{18–20} both causing higher cost and CO₂ emissions than conventional reinforcing bars. Furthermore, the use of concrete types that require more cement (UHPFRC,^{18,20–22} 3D-printed concrete^{16,24}) contradicts the aim to produce sustainable structures. Both issues will limit the immediate impact on the mass market, since conventional RC has proven to be a cost-effective technology that also serves as a structurally safe and fireproof solution with established recycling loops.

Consequently, this study explicitly targets the use of widely available technologies for concrete and reinforcement while introducing a different formwork concept: polymer-based 3D-printed formwork (introduced in²⁸ for columns) is used to produce various specimens representing essential parts of a material-efficient, ribbed concrete slab. This study focuses on the structural design of a material optimized slab structure as well as specimen testing, while the fabrication and design of the formwork are covered elsewhere.²⁹ The necessary structural design steps for solid and ribbed slabs are discussed (Section 2) and integrated into a digital design-to-production workflow for optimized ribbed slabs using 3D printed formwork (Section 3). Finally, specimens representing full-scale parts of the case study (ribs, slab-column transition)

TABLE 1 Overview of concrete floor slabs manufactured using digital processes.

Project Name	Formwork			Concrete Type	Reinforcement Type
	Technology	Properties	Material		
Fast complexity ¹⁶	BJ	Reusable	Sandstone with PE coating	Printed	Shell: CFRP-mesh, ribs: post-tensioning
Smart slab ¹⁷	BJ	Disposable	Sandstone with PE coating	Sprayed	Shell: fibers, ribs: rebars, posttensioning
Funicular floor slab 1 ¹⁸	CNC cutting	Disposable	EPS	Cast (UHPFRC)	Fibers, ^a
Funicular floor slab 2 ¹⁹	CNC cutting, FDM (soffit, HVAC)	Stay-in place; insulation, HVAC	PLA, EPS	Cast	^a
Hilo (slabs A/B) ²⁰	Top: CNC cutting Bottom: A: CNC cutting B: BJ	A/B: stay-in-place; insulation, B: HVAC	Top: polyurethane foam mounted on OSB Bottom: A: LDPE, PVC profiles B: sandstone PLA for ducts	Cast (UHPFRC)	Posttensioned internal ties
FoamWorks ²¹	FDM	Disposable insulation	Mineral foam (fly-ash)	Cast (UHPFRC)	Fibers
Smart takes from the strong ^{22,23}	BJ	Permanent	Sandstone	Cast (UHPFRC)	Fibers
COEBRO ²⁴	3DCP	Permanent, concrete cover	Printed concrete	Cast (SCC)	Rebars
Eggshell: ²⁹ and in this study	FDM	Disposable	Polymer (PLA)	Cast (SCC/NC)	Rebars

^aTies or stiff bearings needed for absorption of horizontal forces.

are produced and structurally tested as proof of concept (Section 4).

2 | STRUCTURAL DESIGN OF CUSTOMIZED TWO-WAY RIBBED RC SLABS SUPPORTED ON COLUMNS

2.1 | General

Floor slabs must ensure structural safety by resisting the design loads with sufficient ductility, and also comply with serviceability criteria by limiting deflections, cracking and stresses. This section presents the most important structural requirements for customized two-way ribbed slabs supported by columns (Figure 3): longitudinal reinforcement design and depth determination, as well as the design against punching, fire and deviation effects of curved reinforcement. Note that the latter are particularly

relevant (fire) or unique (deviation forces) to optimized ribbed slabs.

2.2 | Design of longitudinal reinforcement

While linear-elastic FEA can adequately approximate the behavior of a two-way slab under service loads, designing longitudinal reinforcement to ensure structural safety based on linear-elastic results typically leads to unrealistic and uneconomical reinforcement.³⁰ However, due to its simplicity and time efficiency, this approach is preferred by most designers today. Ideally, the load-bearing capacity of a two-way reinforced structure should be analyzed based on the theory of plasticity. Full plastic solutions were already available many decades ago using the advanced strip method or the equivalent frame method (lower boundaries)³¹ (Figure 3a) or the yield lines method (upper boundary)³² (Figure 3c). While both

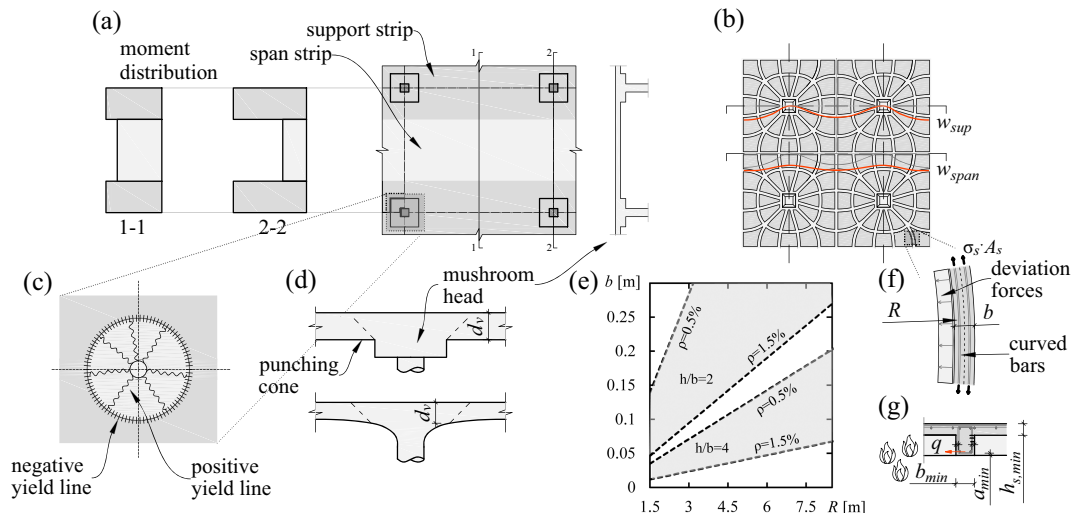


FIGURE 3 Structural design of two-way slabs supported on columns: (a) moment distribution with equivalent frame method; (b) deflections; (c) yield line mechanism at column region; (d) punching at mushroom slabs; (e) cracking-safe rib width for curved ribs; (f) deviation forces caused by curved ribs; and (g) lower dimensioning limits for fire resistance.

methods are easy to use for basic geometries, reinforcement layouts and load cases, their application is tedious in more general cases. The incorporation of elastic-plastic analysis in finite element software would be preferable for such situations, in order to accurately account for effects such as the locally increased depth at mushroom slabs which (a) reduces the required flexural reinforcement while (b) increasing the stiffness. However, in daily engineering practice, the related modeling effort and calculation time are commonly still regarded as excessive.³⁰

2.3 | Design for limiting deflections

The primary goal of floor slab design is to provide large spans while maintaining low depths. Rules of thumb typically consider the member height h (or depth d) as a function of the span l , with deflection limits as theoretical background. EC2³³ recognizes this concept by an indirect check, indicating specific span-to-depth ratios (l/d) for various static systems and support conditions (Figure 3b). In EC2, a maximum long-term deflection of $w_{\max} = l/250$ under quasi-permanent loads is generally required for RC buildings. Estimating long-term deflections must take into account the effects of cracking, shrinkage and creep. However, reliably predicting the long-term behavior of concrete and its effect on the actual deflections is not straightforward. A commonly used approach to account for the lowered stiffness properties caused by creep consists in increasing the deflections evaluated in the uncracked state, that is,

$$w_{c\varphi} = w_c \cdot (1 + \varphi) \quad (\text{m}), \quad (1)$$

where $w_{c\varphi}$ is the long-term deflection in the uncracked state in m; w_c is the deflection due to permanent loads in the uncracked state in m and φ is the creep coefficient. Equation (1) typically defines a lower boundary for the deflections.

A better approximation could be obtained by considering cracked cross-sections and in addition to creep. However, determining the cracked-elastic stiffness is not straightforward, particularly in the case of torsional moments.³⁴ Since in reality, a structure behaves between the uncracked and fully cracked states, the deflections are typically estimated based on the uncracked state in practice (Equation 1), increased by multipliers accounting for multiple effects at the same time. More severe deflection limits could be considered for designing on the safe side. Deflections caused by dead loads might be compensated by formwork camber, which could be easily incorporated by customized formwork methods.

2.4 | Design against punching

Slabs supported on columns must be designed to prevent punching failures, for example using the corresponding design equations of fib Model Code 2010³⁵ (see Section 4.5.1). In solid slabs, the required resistance can be achieved either by designing punching reinforcement or by increasing the depth around the column (mushroom slabs, Figures 1c and 3d). To avoid punching failures, ribbed slabs are also designed with solid parts around columns. The area of these solid parts can be

chosen by determining the required circumference where the punching resistance without punching reinforcement is sufficient. The principle of increasing the total slab depth or designing mushroom column heads could also be applied. Alternatively, using shape freedom provided by 3D printed formwork, the ribs can smoothly transition to the column, as exemplified in our design (Section 3).

2.5 | Design of curved ribs

As mentioned, the shape freedom provided by modern formwork technologies could be used to design expressive structures like those proposed by Arcangeli⁴ (Figure 1b) again today. His approach was to provide ribs aligned with the structure's principal bending moment trajectories, thereby converting a solid slab into a ribbed structure. Torsional moments in the resulting ribbed structure vanish under identical loading and support conditions as those used to determine the directions of the principal bending moments of the solid slab.³⁶ Nonetheless, ribs curved or kinked in plan cause deviation forces (Figure 3f) at the level of the rib's tension (or compression) chord which are locally concentrated in the case of kinks. Thus, in order to avoid the corresponding transverse bending moments, it is best to provide diaphragm ribs at kinks resisting the deviation forces. For a continuously curved rib subjected to a sagging moment, the deviation force q per unit length can be approximated by

$$q = \frac{M_{\text{rib}}}{R \cdot z} = \frac{\sigma_s \cdot A_s}{R} \approx \frac{8 \cdot \Delta \cdot \sigma_s \cdot A_s}{s^2} \quad (\text{MN/m}), \quad (2)$$

where R is the rib radius in plan in m, z is the inner lever arm in m, σ_s is the tensile stress in the reinforcement in MN/m^2 , A_s is the cross-section of the reinforcement in m^2 , Δ is the sagitta and s is the secant, both in m.

The transverse bending moments—which correspond to torques acting on the ribs, as required to ensure that the principal bending moment direction remains aligned with the curved (or kinked) rib axis—can be estimated by multiplying the deviations forces (2) by the tension chord's lever arm e with respect to the web and slab transition ($m_{\text{trans}} = q \cdot e$). On the other hand, the cracking moment m_{cr} per unit length of a rib can be estimated by:

$$m_{\text{cr}} = \frac{f_{\text{ctm}} \cdot b^2}{6} \quad (\text{MNm/m}), \quad (3)$$

where f_{ctm} = mean tensile strength of the concrete in MN/m^2 and b = rib width in m.

By equating $m_{\text{trans}} = m_{\text{cr}}$ using Equations (2) and (3), assuming a fully yielding reinforcement ($\sigma_s = f_{\text{sy}} = 500 \text{ N/mm}^2$) and a lever arm $e \approx 0.8d$, the width of the rib b that avoids cracking under lateral loads can be obtained for different h/b -values and reinforcement ratios ρ for each rib radius R in plan (Figure 3e).

2.6 | Design for fire resistance

The mechanical properties of concrete and reinforcement are affected by fire exposure and high temperatures. In particular, the strength of reinforcing bars is severely reduced when heated to 600°C (loss of 50% of yield stress for reinforcing bars between 400° and 600° , and even a loss of 70% for prestressing steel³⁷). As a result, reinforcement must be protected by concrete to maintain its load-bearing function for a specific duration of fire exposure (e.g., R180, load-bearing resistance for 180 min). This is particularly relevant for ribbed slabs, since the ambition to save material results in increased exposed surface, thinner elements and reduced concrete cover in the lateral direction. The Eurocode EN1992-1-2 for structural fire design³⁷ provides tabulated (deemed-to-satisfy) values for recognized design solutions of various structural elements for fire exposures of up to 240 min. Lower limits for slab height, rib width and concrete cover are given for ribbed floor slabs, taking into account the static system, spanning direction and type of reinforcement considered (Figure 3g). Exemplary values for REI60, the typical fire resistance class for office buildings and housing, include a rib width $b_{\text{min}} = 120 \text{ mm}$ and a minimum bar axis distance $a_{\text{min}} = 25 \text{ mm}$, which could be further reduced to $b_{\text{min}} = 100 \text{ mm}$ for $a_{\text{min}} > 35 \text{ mm}$. The minimum slab thickness of the flange h_s is specified as 80 mm.

3 | CASE STUDY: DIGITAL DESIGN AND PRODUCTION OF A MATERIAL OPTIMIZED SLAB WITH 3D PRINTED FORMWORK

3.1 | Description of the case study

This chapter addresses the design and production of material optimized RC slabs with digital tools. A general methodology is first introduced, which details are then discussed for an exemplary slab. The case study consists of a multibay office building with 8 m spaced columns. The case study slab is subjected to a dead load of 2.0 kN/m^2 and a variable load of 3.0 kN/m^2 (common values for office buildings and in accordance to³⁸), which

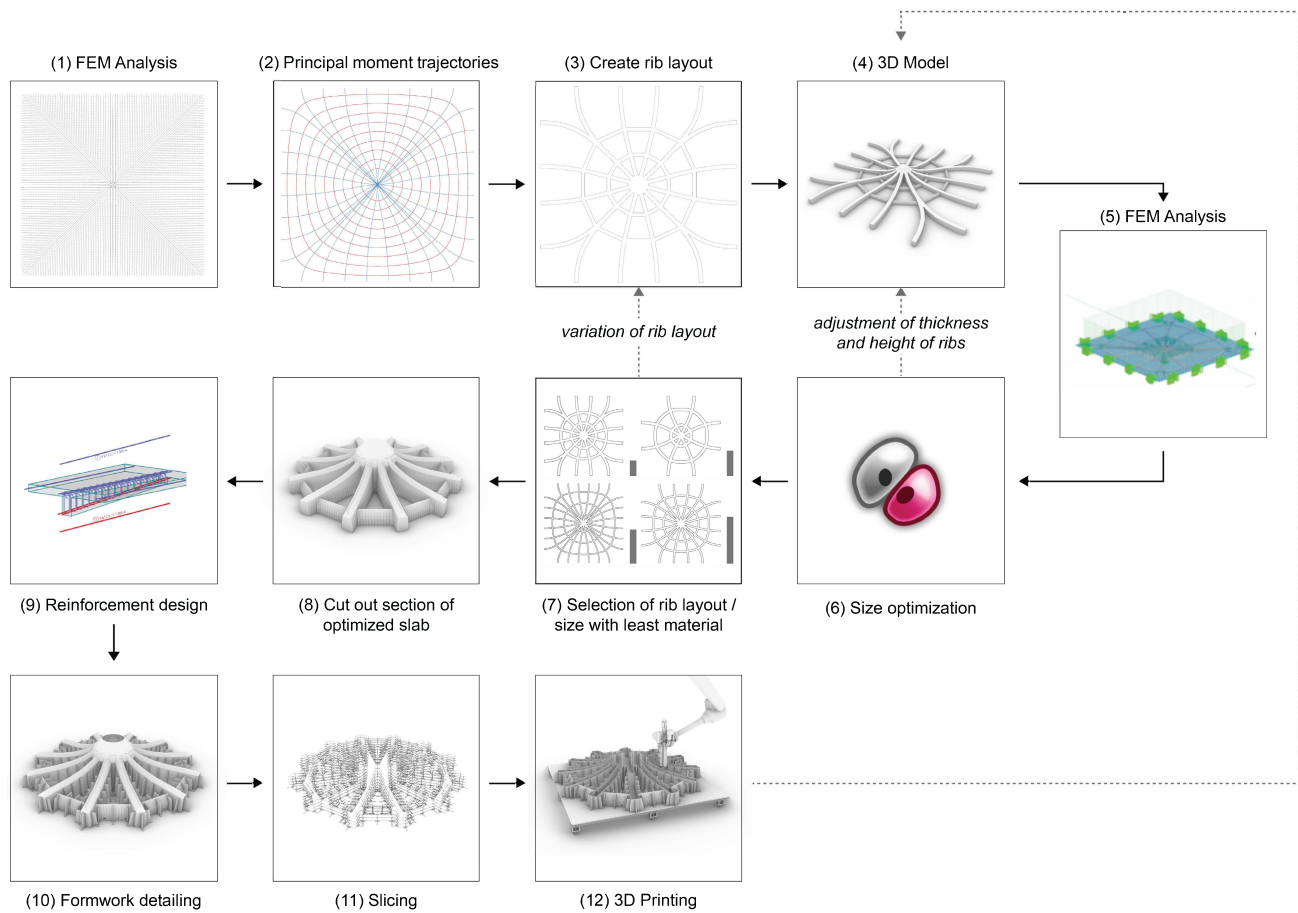


FIGURE 4 Digital design-to-fabrication workflow (also in²⁹).

results in a quasi-permanent load of ca. 3.0 kN/m^2 ($\psi_2 = 0.3^{39}$). The slab is required to provide a fire resistance of 60 min and a maximum long-term deflection under quasi-permanent loads below $L/300$. The long-term deflection is calculated based on the linear-elastic FEA results using Equation (1) with $\varphi = 2.5$.

3.2 | Digital design-to-production workflow

A research gap was identified as structural design and planning of additive manufacturing fabrication should go hand-in-hand.⁴⁰ To target this research gap, a holistic digital design-to-production workflow was developed within this study. The workflow is outlined in Figure 4, with the details being presented in Appendix A. The details of structural design, structural analysis and size optimization of tailored ribbed floor slabs are discussed in the following, while the link to automated formwork production of the element is discussed in greater detail elsewhere.²⁹

3.2.1 | Structural requirements informing the design

The workflow introduces the relevant structural design steps (Section 2) that inform the final structure (Figure 5a). The model parameters are visualized in Figure 5b, and the respective limits are introduced to the parametric design code (Step 4 in Figure 4 and Appendix A). Fire regulations (R60) limit the minimum rib widths (b_1 , b_2) and slab height (h_s) to 120 mm and 80 mm, respectively.³⁷ The slab height (h_s) is further limited by taking into account the span-to-depth values for the indirect deflection check ($l/d < 30$ for interior spans of two-way slabs³³), which are dependent on the respective rib spacings (s_1 and s_2 , set in advance). The rib curvature ($R_{1,\max}$, $R_{2,\max}$) also informs the rib widths (b_1 , b_2) to mitigate transverse bending effects caused by deviation (Section 2.5). The deflection of the entire structure informs the required height of the primary ribs (h_1) (Section 3.2.3). The depth variation (h_c) in the column region was chosen to provide a continuous force flow.

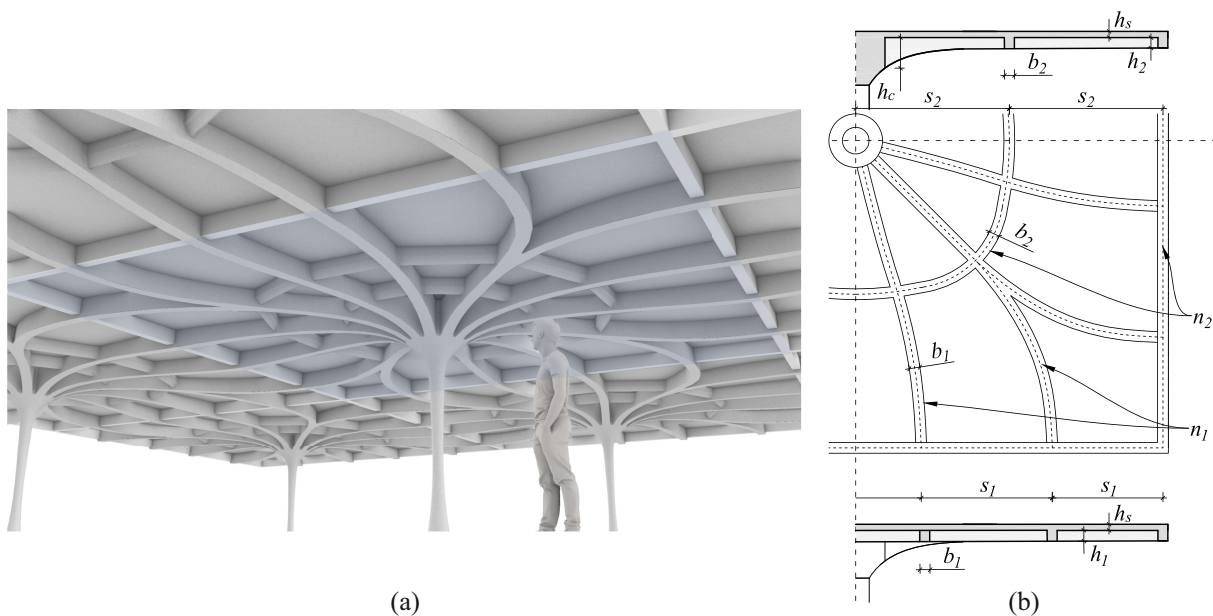


FIGURE 5 Multibay office building with 8 m spans: (a) visualization of design achieved by the parametric model and (b) design parameters.

3.2.2 | Integration of FEA for slabs in digital production workflows

The visual programming language and environment Grasshopper,⁴¹ which runs within the computer-aided design application Rhinoceros 3D (v7),⁴² is used for parametric design. The commercial FEA-software Dlubal RFEM (v5.61)⁴³ is used for the structural analysis of the structure assuming linear-elastic behavior (Step 5 in Figure 4). The FE-model is a rectangular section of the slab, including the top of the column and half a span on each side. The edge conditions represent the midspan situation for symmetrical loading, with rotation around the edge axis restricted but vertical deformations permitted. Note that Sofistik (via interface) and the Grasshopper plug-in Karamba⁴⁴ are two other possible solutions for FE-analysis in conjunction with Grasshopper; however, Karamba currently only supports beam and shell elements, preventing its use for this study. On the other hand, Dlubal already has a COM interface for exchanging Rhino-designed models, with the ability to assign structural properties to elements (e.g., beam, surface) and add loading conditions (supports or hinges). However, fully integrating the FEM-solver in Grasshopper was impossible because some processing and FEM calculations must be performed within the RFEM software (load-cases, FE-mesh generation, calculation). The B + G Toolbox,⁴⁵ integrated in the meantime in RFEM, is an interface between the mentioned programs allowing these missing steps to be integrated into Grasshopper. As a result, additional Grasshopper plug-ins such as the solver

Galapagos⁴⁶ can be applied, facilitating the programming of parametric optimization loops.

3.2.3 | Introduction of size optimization

Galapagos is used to minimize the primary rib height (h_1) for a given rib layout with equally spaced ribs at the edges (s_1) while meeting a long-term deflection criterion ($w_{\max} = L/300$) under quasi-permanent loads (Steps 6 and 7 in Figure 4). To find the optimal solution in terms of concrete consumption, four models with different amounts of equally spaced primary ribs ($n_1 = 2, 4, 6$, or 8) per edge are calculated separately for this study (Step 8 in Figure 4). To demonstrate concrete grading potential for lower carbon emission, the concrete class is chosen separately for the ribs (C50/60) and the slab (C25/30). The primary ribs are complemented by circumferential secondary ribs, and a rectangular grid along the midspan sections. By comparing the concrete masses m_c , the optimal solution is found. The comparison results neglects overlapping parts of the modeled structure (e.g., colliding surfaces).

The results in Table 2 show that an optimal solution is found with four ribs per side. A higher number of ribs leads to higher material consumption despite a lower construction height. A comparison of concrete masses with a solid slab is included to evaluate the optimization grade. The height of the solid slab was chosen to provide the same linear-elastic midspan deflections assuming a concrete class of C25/30. Note that for the ribbed slabs,

TABLE 2 Geometrical parameters and calculated concrete masses for several configurations of RC floor office slabs with 8 m span.

Type	n_1 (–)	s_1 (m)	h_c (m)	h_s (m)	h_1 (m)	$h_{tot} =$ $h_s + h_1$ (m)	b_1 (m)	b_2 (m)	m_c (t)	% (–)	$\Delta\%$ (–)
Solid slab	-	-	-	-	-	0.22	-	-	35.2	100	
Curved ribbed	2	2.67	0.40	0.115	0.21	0.33	0.14	0.12	23.1	66	–34
Curved ribbed	4	1.60	0.38	0.080	0.20	0.28	0.14	0.12	20.9	59	–41
Curved ribbed	6	1.14	0.36	0.080	0.18	0.26	0.13	0.12	22.7	65	–35
Curved ribbed	8	0.89	0.36	0.080	0.18	0.26	0.12	0.12	24.8	71	–29

Note: Bold values were used to indicate the optimal solution, which in the end was also chosen for the prototype and for the comparison to a reference slab which is also bold.

m_c includes the approximate mass of the column head due to the modeled ribs. Consequently, the mass (~ 0.1 t) of a circular column head was added to the solid slab for comparison. When comparing the optimized design to a statically equivalent solid slab on a structural scale, a concrete reduction of approximately 40% is thus achieved (see bold rows in Table 2).

3.3 | Applied 3D printing formwork technology

The “Eggshell” technology²⁸ was further developed in this project to be applied to ribbed slab structures. The original technology involves 3D printing ultra-thin (1–2 mm) plastic formworks and casting with a set-on-demand concrete process to minimize formwork pressure. This method allows for very high geometric resolution⁹ and the use of conventional reinforcement. Considering the cement consumption and the process reliability, it is preferable to use standard concretes or even low-carbon concrete instead of set-on-demand concrete in slab structures. However, the correspondingly higher formwork pressure must be considered. As a result, the rib formwork was designed with a slightly increased thickness (4–5 mm) and additional printed stiffeners²⁹ (Step 10 in Figure 4). The fabrication workflow entails processing the desired geometry within the COMPAS Python framework,⁴⁷ including slicing with COMPAS SLICER⁴⁸ and robotic print path generation using COMPAS RRC⁴⁹ (Steps 11 and 12 in Figure 4). The data is then sent to a six-axis robot, which carries an extruder for the FDM process.

3.4 | Production of slab sections with 3D printed formwork

Geometrically complex shapes are easily enabled by formwork printing, which can provide smooth transitions

between different structure parts inspired by the force flow. These shapes can be inspired by nature (biomimetic, Figure 1a), result from the application of structural principles (Figure 1b,c) or be generated by computational form-finding processes (e.g., topology optimization). Punching failures in point-supported slabs can be avoided by providing variable depth ribs, distributing the concentrated column reaction (Figure 6c, similar principle in Figure 1c). The latter is verified in this study by structurally testing a slab-to-column demonstrator with 12 ribs merging into a circular column (Figure 6a–c).

A separate set of tests is performed to verify the design of curved or kinked ribs. Deviation forces are caused by the tension and compression chords of the ribs, causing transverse bending moments that must be considered in design (see Section 2.5), for example, by providing diaphragms or limiting the rib curvature in plan. These tests consist of three separate ribs specimens with a constant height but different shape (straight, kinked, curved), each representing a typical section of a point-supported ribbed slab (Figure 6d–f).

All specimens (slab-to-column transition and separate ribs) were produced upside down. The plastic formwork for the rib parts was produced first, with all specimens using 3D printed formwork (see²⁹ for detailed information on the formwork design and construction process). The formwork was removed after casting the ribs, and the solid part of the slab was cast on a second casting day using conventional wood formwork frames. The ribs-slab construction joints were printed with a certain roughness to allow force transfer between parts cast at different times.

4 | EXPERIMENTAL CAMPAIGN

4.1 | Description of specimens

The reinforcement of the slab-to-column specimen (S1) consisted of prefabricated cages for each rib (mean

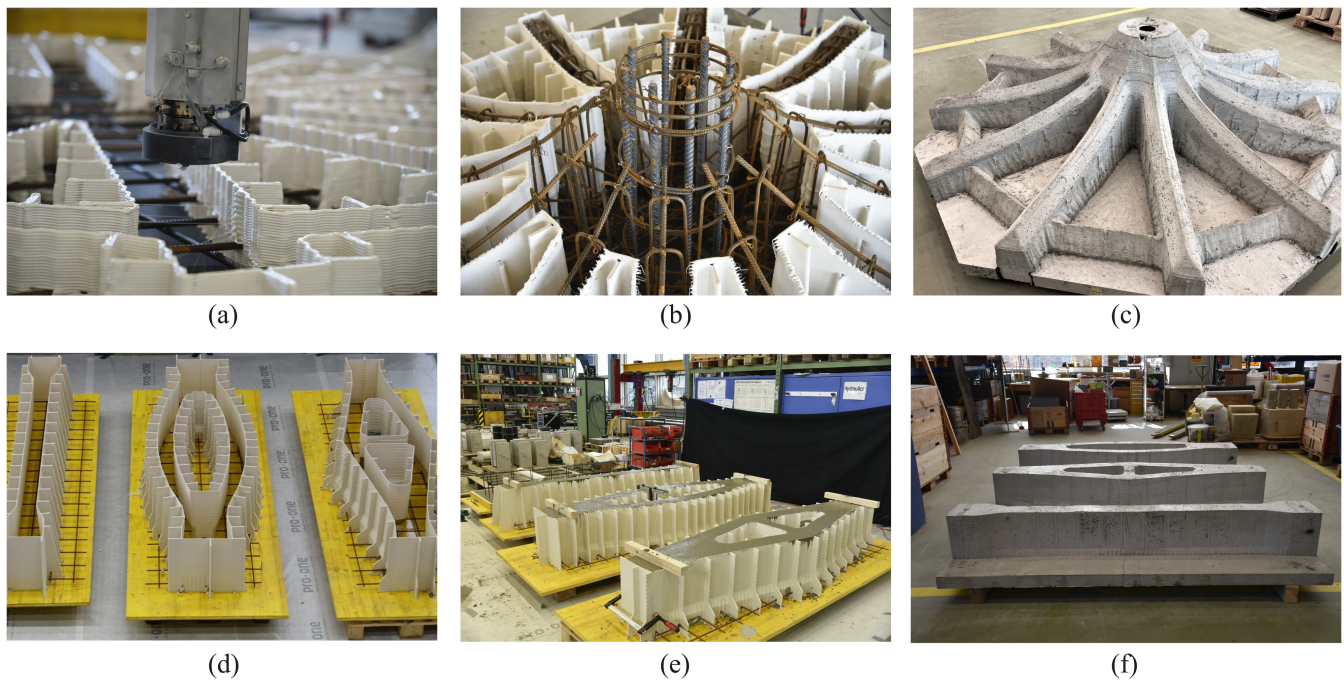


FIGURE 6 Specimen production (upside down): (a)–(c) slab-to-column transition, showing formwork printing with stiffeners; reinforcement cage integration and specimen after demoulding, respectively; and (d)–(f) ribs, showing printed formwork with stiffeners before and after casting, and after demoulding, respectively.

rib width $b = 140$ mm, Figure 6b) and a reinforcement mesh for the solid part of the slab (Figure 6c). The secondary ribs were unreinforced. In addition, a column reinforcement cage was provided at the center (Figure 6b). The rib reinforcement cages were straight in plan but had a variable height. The longitudinal bottom (in casting position) reinforcement consisted of an orthogonal mesh $\text{Ø}10@150$ mm in the slab with two additional radial bars $\text{Ø}8$ in each rib (Figure 7a). To provide splicing of the latter, 12 additional $\text{Ø}8$ bars were placed orthogonally in the column transition region. The rib cages were designed with two-legged stirrups $\text{Ø}8@200$ mm. To avoid colliding with the extruder while printing the top (in casting position) formwork (“roof”), the stirrup height was set 10 mm lower than the rib height without the triangular roof. Specimen S1 had a total height of 700 mm and a mass of 2.94 t. The total reinforcement mass was 142.2 kg (118 kg/m^3 concrete), and 125 kg (106 kg/m^3) without column reinforcement, respectively.

For comparison, an additional solid slab (S2) with a constant thickness was produced and tested. The slab was designed according to EC2 for the same case study as the ribbed slab (Section 3.1). The depth of the slab (220 mm) was chosen to provide the same maximum linear-elastic deflection as the ribbed slab. The longitudinal reinforcement was designed to provide sufficient flexural capacity yielding an orthogonal mesh $\text{Ø}14@150$

(Figure 7b). With fixed parameters of depth and longitudinal reinforcement, the punching reinforcement was designed following the EC2, which allows the punching resistance attributed to the concrete only to be increased by a maximum of 100% by the application of shear reinforcement (note that some countries propose even lower limits). The contribution was fully utilized through the design of eight reinforcement cages with two-legged stirrups ($\text{Ø}8@150$ mm). The calculated punching resistance according to EC2 ($V_{\text{Rd,EC2}} = 686 \text{ kN}$) was still below the applied loads in the case study ($V_{\text{Ed}} = 936 \text{ kN}$, without eccentricities) and a punching failure of the slab section around to the column is expected. The specimen had a mass of 3.33 t and contained 113.7 kg (86 kg/m^3 concrete). It should be noted that the missing bottom reinforcement (at the top of the slab in casting position) should be considered for comparison purposes. Assuming an $\text{Ø}8@150$ mesh results in additional 24.2 kg/m^3 for this section, thus a total of 110.2 kg/m^2 , which is comparable to specimen S1. Despite the designed ribbed slab uses 40% less material than the equivalent solid slab, the material use in the fabricated section close to the column is similar in both cases.

The reinforcement cages for the ribs were made by a prefabrication plant, testing the needed fabrication possibilities and needed tolerance of curved and kinked cages for placement into the printed formwork. Polygonally

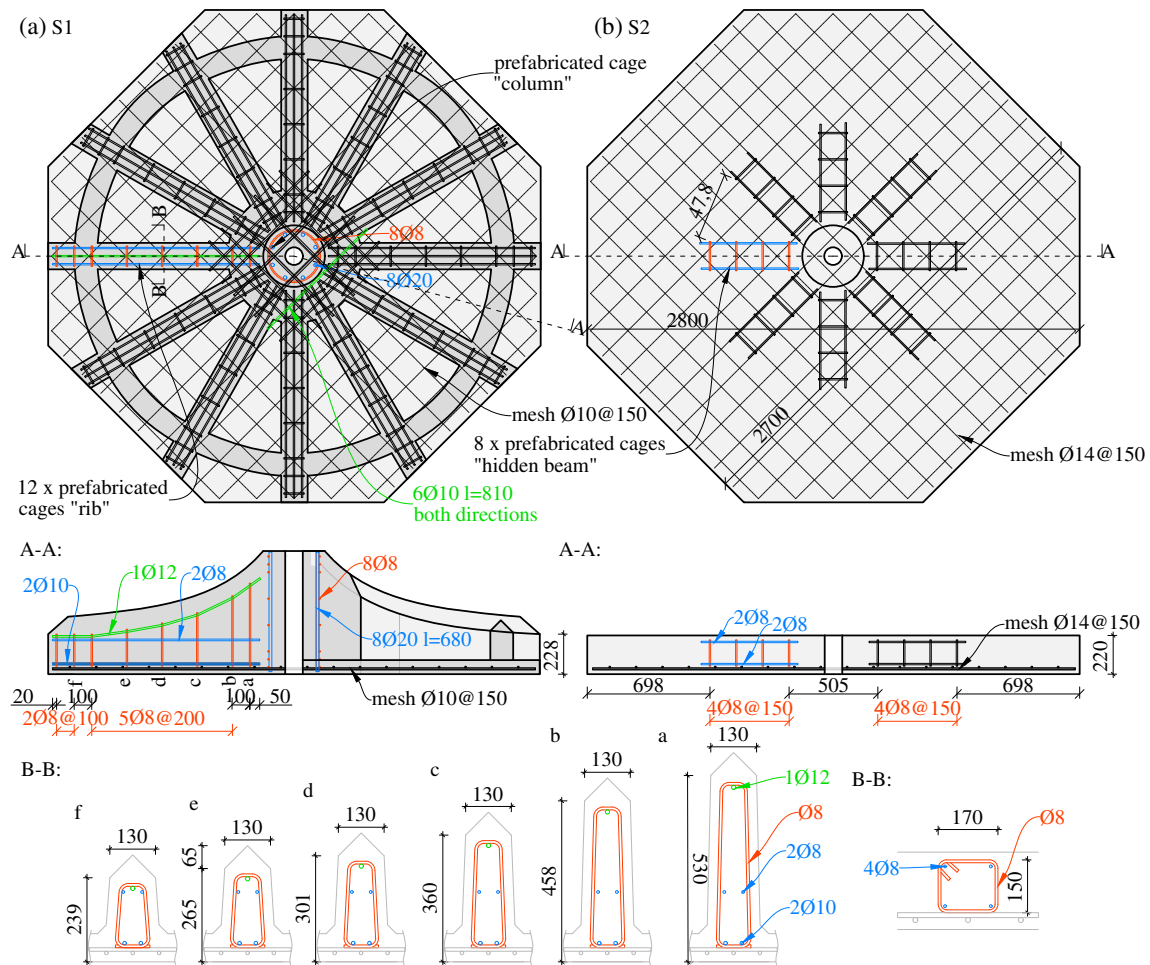


FIGURE 7 Reinforcement layout of the specimens (a) S1: transition from slab-to-column and (b) S2: solid slab specimen.

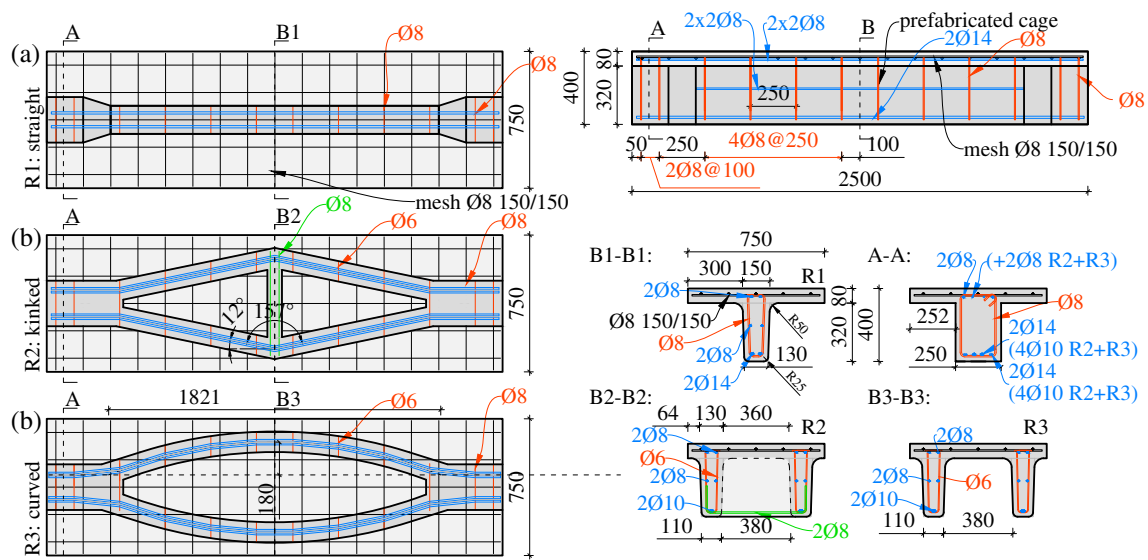


FIGURE 8 Reinforcement layout of the rib specimens: (a) R1 straight rib; (b) R2: kinked rib with a diaphragm; and (c) R3: curved rib.

bent bars with Ø12 mm could be produced automatically, as idealizations of the continuous formwork curvatures. A prewelded mesh was used to reinforce the slab. Figure 8 illustrates the reinforcement layout.

The ribs were designed aiming for the smallest possible rib width while providing code-compliant anchorage of two-legged shear reinforcement.³³ Another requirement was that they be strong enough to stay-in-place during transport and formwork placement. A minimum rib width of 110 and 130 mm could be achieved with stirrups Ø6 mm and Ø8 mm, respectively. The concrete cover was planned with 20 mm with an additional 10 mm tolerance on each side. The transverse reinforcement a_{sw} in the straight and curved (kinked) web was 402 and 452 mm²/m, resulting in reinforcement ratios of $\rho_w = 0.32\%$ and 0.21% , respectively. The longitudinal top (in casting position) reinforcement of the straight (curved) ribs was $A_s = 307(314)$ mm², corresponding to geometrical reinforcement ratios of $\rho_s = 0.68(0.41)\%$. The bottom reinforcement amounted to $A_s = 351(452)$ mm², that is, $\rho_s = 0.77(0.59)\%$. The measured specimen mass was 0.75 t for the straight rib specimen and 1.0 t for the other two specimens.

TABLE 3 Mechanical properties of the reinforcing steel bars.

Ø (mm)	E_s^a (GPa)	f_{sy} (N/mm ²)	f_{su} (N/mm ²)	ϵ_{su} (‰)
8	195.4 (±0.5%)	514 (±0.9%)	608 (±0.6%)	47.3 (±7.1%)
10	196.1 (±2.0%)	525 (±1.9%)	607 (±1.9%)	55.2 (±12.8%)
12	196.3 (±2.0%)	505 (±0.1%)	590 (±0.3%)	61.7 (±11.8%)
14	192.6 (±3.8%)	522 (±1.4%)	620 (±0.7%)	109.4 (±9.6%)

^a E_s was evaluated with the measurements at $\sigma = 120$ and 360 MPa, respectively.

TABLE 4 Mechanical material parameters of concrete.

Specimen	Part	Type	D_{max} (mm)	Age (days)	f_{cm} (N/mm ²)	$f_{cm,cube}$ (N/mm ²)	f_{ctm} (N/mm ²)
Ribs (R1–R3)	Web	C50/60SCC 3708CL	8	25	56.2 (±1.0%)	61.1 (±0.9%)	4.8 (±2.7%)
Ribs (R1–R3)	Slab	C50/60SCC 3708CL	8	21	57.9 (±1.3%)	61.6 (±1.4%)	4.3 (±3.5%)
Slab/column (S1)	Web	C50/60SCC 3708CL	8	44	71.0 (±2.4%)	73.7 (±1.5%)	5.4 (±1.4%)
Slab/column (S1) Reference slab (S2)	Slab	C25/30 A151EVO	16	39	35.9 (±2.6%)	42.5 (±1.6%)	3.0 (±4.3%)

4.2 | Material properties

Three tension tests were conducted to determine the mechanical properties of each reinforcing steel diameter (sample length 1.1 m). Table 3 summarizes the obtained material parameters.

All specimens were cast on two separate days to allow for hardening of the ribs and subsequent removal of the printed formwork before the slab part was cast. All specimens were covered with plastic wraps between those castings and at least until 1 week after finalization. The concrete was mixed in the concrete plant and was delivered by truck. For the web of S1 and the rib specimens (R1–R3), self-compacting concrete C50/60 with a maximum aggregate size $D_{max} = 8$ mm was ordered (Holcim 3708CL). A low-carbon concrete C25/30 (Holcim A151EVO) with $D_{max} = 16$ mm was used for the slab part in S1 as well as the reference slab (S2). On both days, samples were cast to determine the material properties. Compression tests on four cylinders ($h/\phi = 300/150$ mm, loading rate = 0.6 MPa/s) and three cubes ($h = 150$ mm; 0.6 MPa/s) were used to determine the mean compressive strength (f_{cm} , $f_{cm,cube}$). Four double punch tests⁵⁰ on cylinders ($h/\phi = 150/150$ mm; 0.02 MPa/sec) were used to determine the tensile strength (f_{ctm}). Table 4 summarizes the mean values of the results with the coefficients of variation.

4.3 | Beam tests on rib specimens

4.3.1 | Test setup and instrumentation

The three rib specimens with different cross-sections described in Figure 8 were tested as beams in three-point bending tests to investigate the structural behavior of ribbed slabs with different rib geometries (Figure 9a). The beams had a span of 2.2 m and a total length of 2.5 m, and were loaded directly over the webs using a hydraulic actuator, using a steel plate (130/130/25 mm)

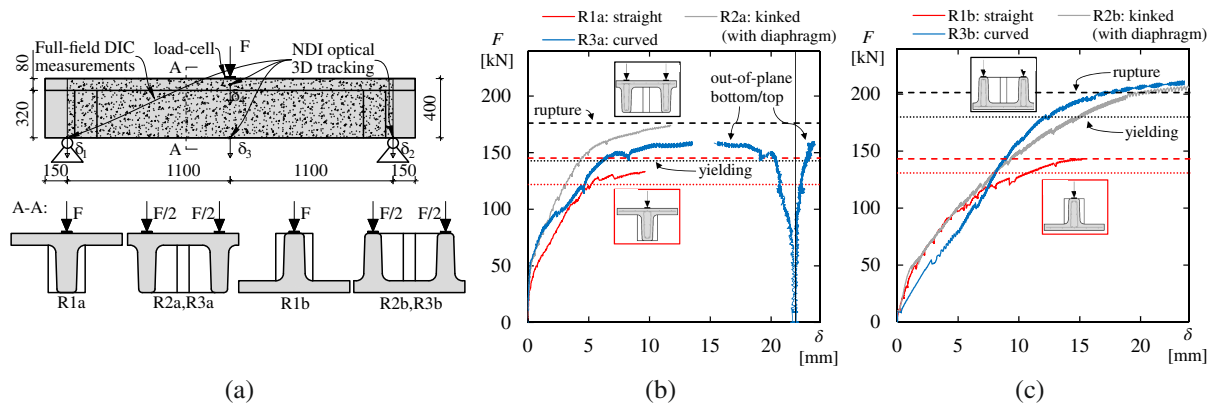


FIGURE 9 Three-point bending beam tests on ribs: (a) test setup; (b) and (c) load-deformation diagrams of tests with ribs in tension (sagging moment) and compression (hogging moment), respectively, and predicted ultimate and yielding capacity (horizontal lines).

as load introduction. The load was increased in a displacement-controlled manner at a rate of 0.1 mm/min. After the flexural reinforcement had yielded, the speed was increased to 0.2 mm/min. Each specimen was first tested in positive bending (Test R1a–R3a: sagging moments, rib acting as tension chord). Subsequently, the specimen was flipped for a second test (Test R1b–R3b: hogging moments, rib acting as compression chord).

The deflections of four different points were measured using a 3D optical measurement system (NDI Optotrak Certus, accuracy 0.1 mm). The relative beam deflection (Figure 9b,c) was calculated deducting the mean deflection of the supports to the midspan deflection. Furthermore, deformations on the beam surface were measured with stereo DIC (2xFLIR 12.3 MP, 4096/3000 px, sensor size 1.1") for tracking crack kinematics. The configuration allowed to cover the whole area between the supports. A load cell and oil pressure measurements within the hydraulic system were used to determine the applied load.

4.3.2 | Results

In both testing configurations, all specimens exhibited a ductile behavior with pronounced plastic deformations, as seen in the load-deflection diagrams (Figure 9b,c). Based on the measurements taken with VIC3D (v9), the crack widths were evaluated using ACDM.^{51,52} Figure 10 shows the crack patterns at maximum load in all tests. The pronounced opening of one or two vertical bending cracks in the region under the load introduction point clearly indicate flexural reinforcement yielding in all tests, except R3a (Figure 10e), where a diagonal crack showed pronounced opening. The crack originated at the section where the two curved ribs merged into a single one.

This specimen with curved ribs, was the most relevant test within this series given it was the proposed solution for the case study (Section 3). The deviation forces of the curved tension chord at the bottom ($R = 2.4$ m, $\Delta = 180$ mm in Figure 8) cause a torque (resulting in torsion in the rib as the principal direction of applied moments is constant) and transverse bending moments in the rib. When compared to the kinked specimen, these effects significantly reduced the stiffness as reflected in the load-deflection curve (compare R2a and R3a in Figure 9b). The first reduction was triggered at 100 kN by the inclined crack and almost reached the top of the beam (Figure 10e). Later in the experiment (~ 150 kN), horizontal cracks appeared in the web, indicating that the transverse bending moments exceeded the cracking moment (Section 2.5). Out-of-plane deformation measurements support these observations by showing twisting (Figure 9b). The effect of the pronounced cracking due to twisting was also visible in the second experiment (R3b), which had a much lower stiffness than the straight (R1b) or kinked (R2b) ribs in the diagrams in Figure 9c. However, it was seen that the ribs' deviation forces in the compression chord could be resisted more efficiently, than in the tension chord as a similar load level as in the kinked rib could be reached under hogging moments (Figure 9c), contrary to the sagging moments (Figure 9b) where the specimen with kinked ribs reached a considerably higher ultimate load. Note that specimen R1 cannot be directly compared, as the width of the single straight rib was less than twice that of the two curved or kinked ribs.

4.3.3 | Analysis of the beam test results

Cross-sectional analysis of the rib specimens was performed using the software INCA2,⁵³ assuming a bi-linear

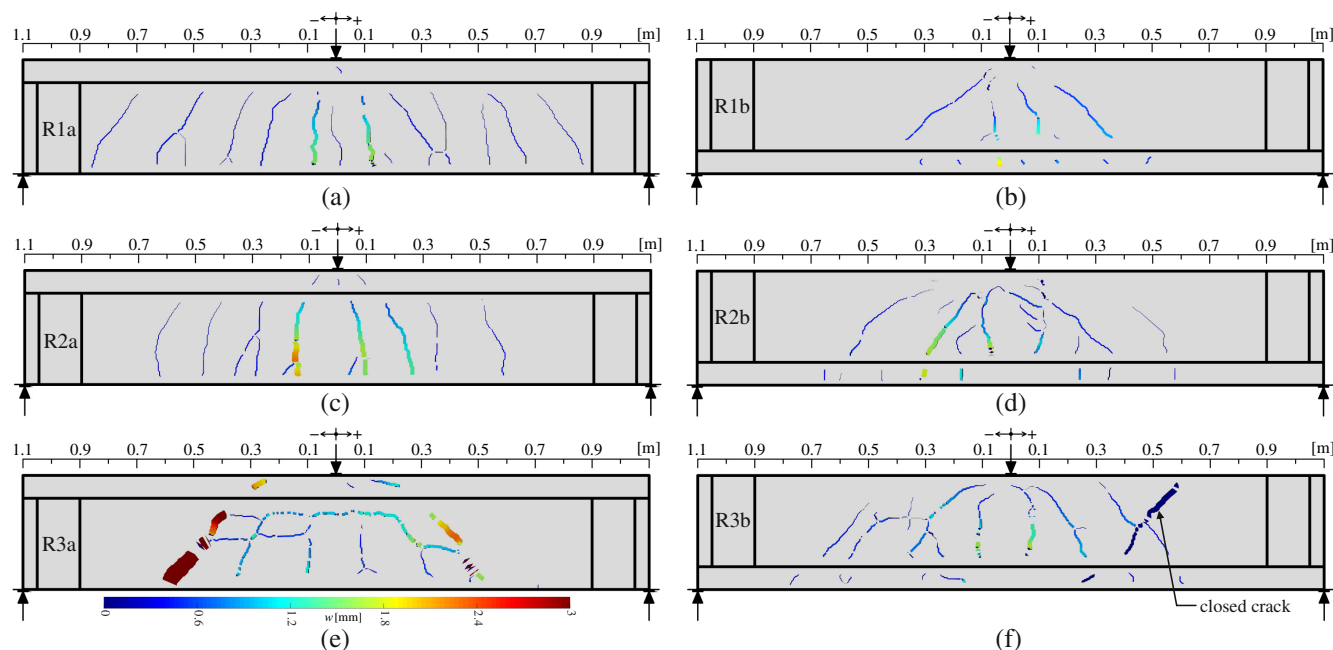


FIGURE 10 Cracking pattern and crack widths determined with ACDM at peak load: (a) R1a; (b) R1b; (c) R2a; (d) R2b; (e) R3a; and (f) R3b.

stress-strain relationship for reinforcement and a parabola-rectangle diagram for concrete under compression with the properties described in the Tables 3 and 4. Hence, an evaluation of the load levels at which (a) the outer and mid-depth reinforcing bars begin to yield and (b) outer bars rupture (F_u), both at midspan was possible. These load levels are indicated in Figure 9b,c, confirming that the reinforcing bars were nearly fully activated. The lower maximum load of R3a, compared to R2a, could be explained by horizontal cracking, and the associated torsional effects, see above. To validate this hypothesis, the horizontal cracking was evaluated with the simplified concept outlined in Section 2.5. The equivalent transverse bending moment m_{trans} per unit length is calculated using Equation (2) based on the evaluated stresses $\sigma_{s,i}$ in the reinforcing bars at a given load level (Table 5). The distances between the axes of the tensile reinforcing bars and the web/flange transition were taken as lever arms e_i .

The transverse bending moment m_{trans} was calculated at $F = 150$ kN, where the load dropped in the experiment (Figure 9b) and horizontal cracking occurred (Figure 10e). The resulting moment considering the contributions of all the reinforcing bars in the rib was 12.8 kNm/m (Table 5), which corresponds well to the calculated cracking moment (Equation 3) at the transition between the web and the flange, which amounts to 13.5 kNm/m. This explains the large out-of-plane deformations observed in the plastic range.

TABLE 5 Estimation of the transverse bending moments in the ribs at load level $F = 150$ kN.

\emptyset (mm)	$\sigma_{s,i}$ (N/mm ²)	e_i (mm)	m_{trans} (kNm/m)
2Ø10	541	284	10.2
2Ø8	525	120	2.6
Total: 2Ø10 + 2Ø8			Σ 12.8

4.4 | Slab tests

4.4.1 | Test setup and instrumentation

The load-bearing behavior of the slab-to-column transition was investigated using structural testing of two slab specimens (S1: ribbed; S2: solid). The test setup is shown in Figure 11. A single point load was applied at the center and increased until failure. The test setup represents a circular section of a multibay point-supported slab with equal spans of 8 m in both directions. The dimensions of the specimen were chosen based on the distance of the points of inflection from the column in a continuous slab (Figure 11a), which lies between 0.12 and 0.22 times the span.⁵⁴ Twelve equally spaced bearings supported the slabs at a distance of 1.2 m from the load, resulting in a radial span of 2.4 m (Figure 11b). Steel plates (120/120 mm) were placed on spherical caps on a PTFE plate to minimize rotational and horizontal restraint by the bearings. The loaded surface was defined by the circular cross-section of the hollow-

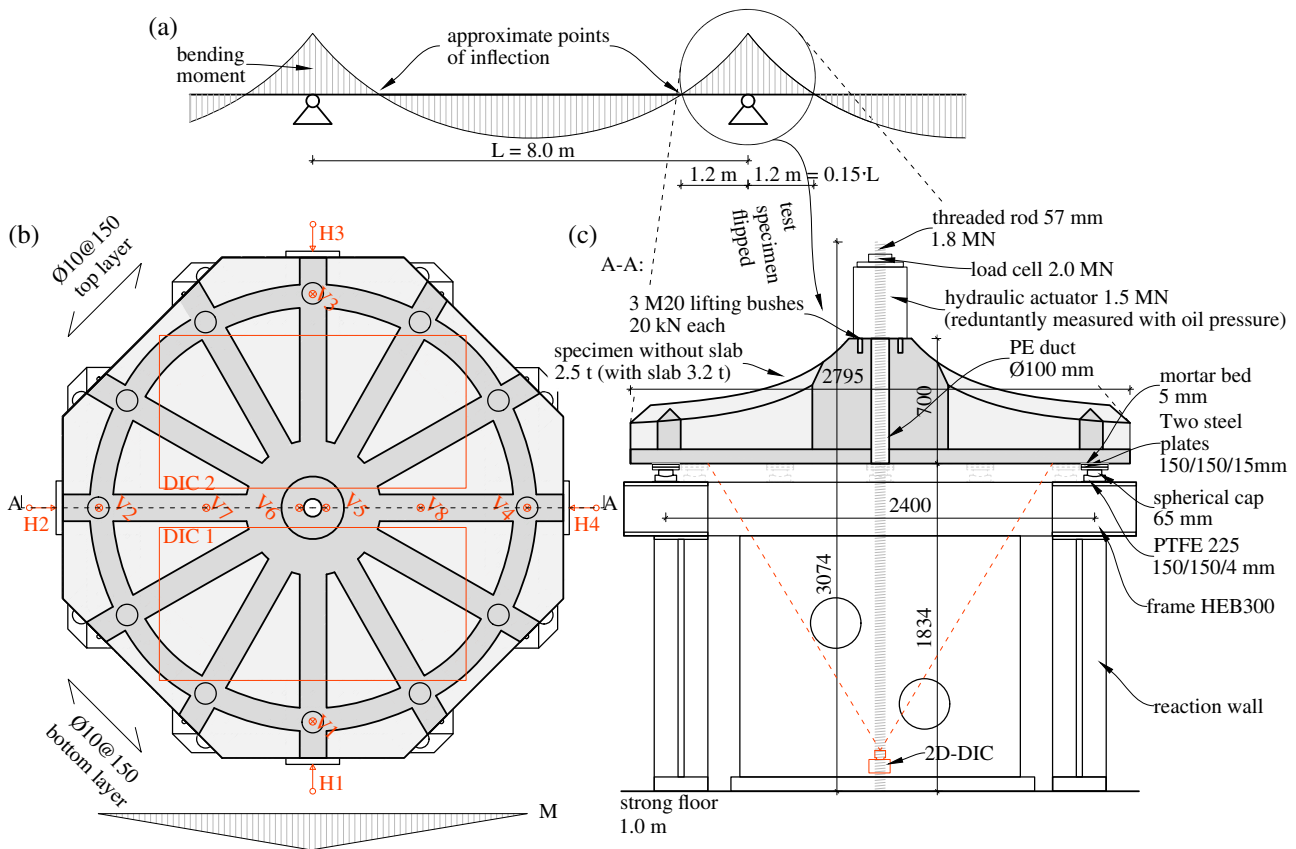


FIGURE 11 Test setup and instrumentation for the slab tests: (a) moment diagram with points of inflection; (b) plan and (c) section A-A.

piston actuator (1.5 MN capacity) that had a diameter of 320 mm. Mortar layers ensured complete contact of the specimen to the support plates and the hydraulic actuator. A hand pump was used to incrementally increase the load with load steps of 50 kN and waiting phases (~5 min) in between.

The applied load was measured redundantly using a calibrated load cell and by back-calculating the measured oil pressure. LVDTs were used to measure vertical (V) and horizontal (H) deformations at several points (Figure 11). Two SLR cameras (Nikon; 3336 × 5032 px) were used to evaluate the cracking pattern at the slab's bottom based on 2D DIC measurements (note that the reduced space below the slab did not allow installing a stereoscopic DIC system as used for the rib tests).

4.4.2 | Load-deflection behavior, cracking and failure mode

The ribbed variant exhibited very stiff behavior (Figure 12a). Until the first cracks appeared at a load of about 500 kN, almost no relative displacements could be measured (mainly the test stand deformed). After initial

cracking, the load could be increased to 1086 kN before the stiffness dropped slightly. The load was then further increased to a maximum load of 1442 kN, with a relative deflection of 6.6 mm (difference of displacements at center and average deformation of the supports). At this deflection, the load dropped slightly, but subsequently remained fairly constant up to a deflection of 16.4 mm, when a radial crack opened suddenly, accompanied by slab reinforcement rupture (Figure 13a). Presumably, this plateau in the load-deflection diagram corresponded to yielding of the slab reinforcement. The governing crack opened at the rib slab joint. Furthermore, rib spalling was visible near the solid column part (Figure 13b) and the cracking pattern at the bottom exhibited significant concrete spallings also at this location (Figure 13c). It should be noted that the spallings at the bottom (tension side) corresponded to the location of the additional reinforcement for splicing (Figure 7a).

The solid slab was loaded until punching failure, which was characterized by a sudden load drop (Figure 12a) and circular cracking around the load introduction (Figure 13d). Circumferential cracking was also observed at the bottom, with a larger perimeter (Figure 13e). Before punching, the load-deflection

FIGURE 12 Test results: (a) load-deformation diagrams; (b) evaluation of solid slab specimen (S2) with the punching provisions of *fib* Model Code 2010.

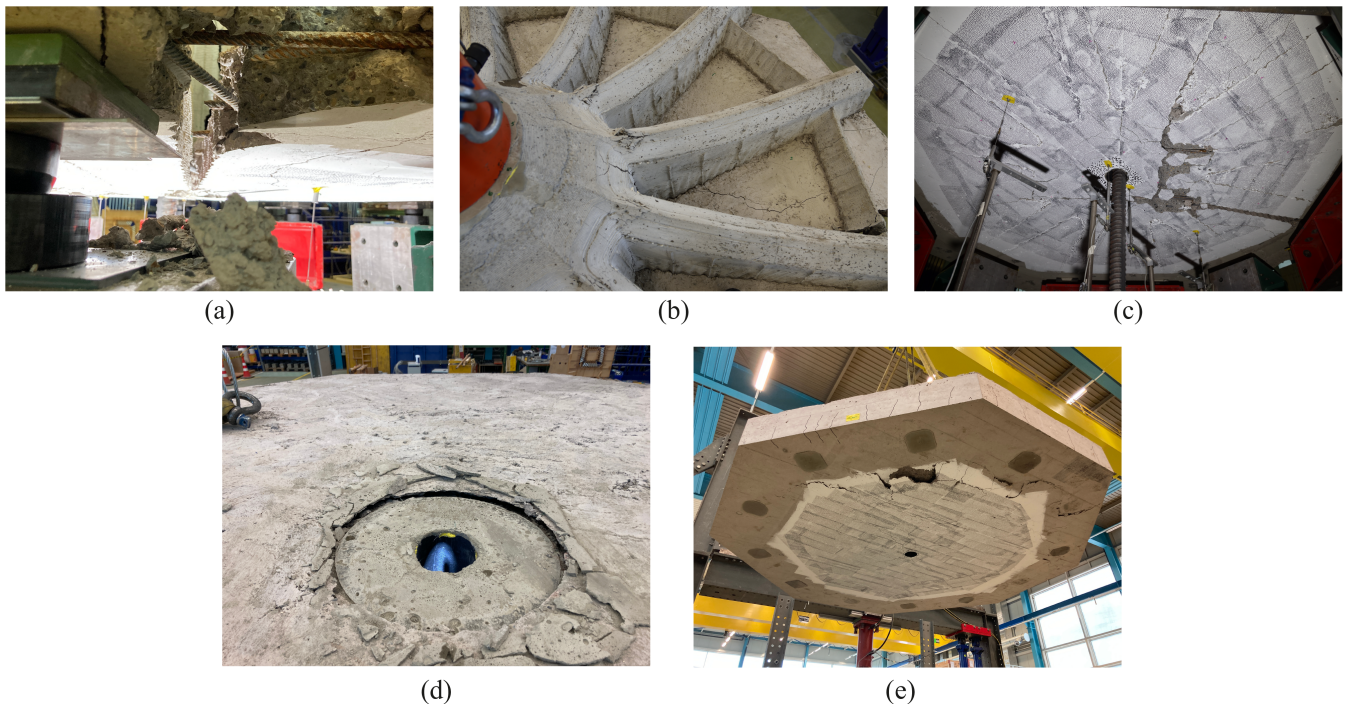
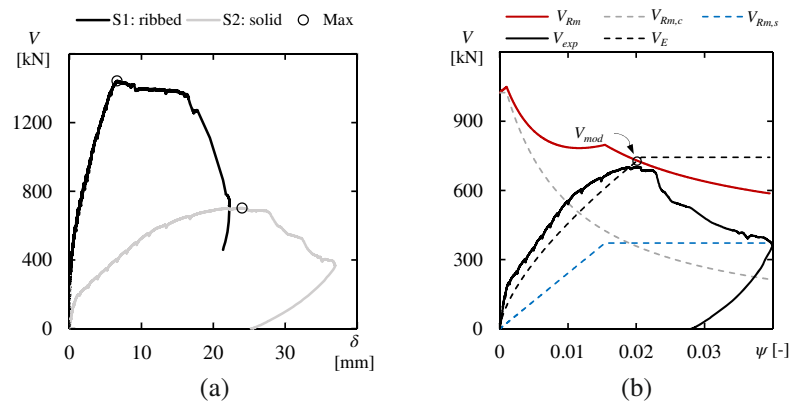


FIGURE 13 Photos of slabs after failure. (a)–(c) ribbed slab S1, showing ruptured bars in the radial failure crack (a), ribs concrete spalling (b), and bottom concrete spalling (c); (d) and (e) solid slab S2, showing punching cone from top (d) and bottom (e).

diagram already softened, presumably due to the loss of stiffness of the reinforcement close to yielding. The maximum load was 702 kN with a relative deflection of 24.0 mm (Figure 12a). The load-rotation ψ_{exp} of the slab is shown in Figure 12b, with the rotation calculated by the vertical displacements (mean of V7–V2, V8–V4 in Figure 11) to compare the load-rotation behavior observed in the tests (Figure 12b), at the maximum load $\psi_{exp} = 0.0204$ was observed.

Based on the deformation and strain fields evaluated with VIC2D (v6), the crack widths at the bottom of each slab were evaluated using ACDM.^{51,52} Figure 14 shows the respective crack patterns at maximum load. The ribbed slab exhibited smaller crack widths than the solid

one, although reaching twice the load. From Figure 14, it is clearly visible that the cracks tend to align with the joints between slabs and ribs (S1) and the longitudinal reinforcement (S2).

4.5 | Validation of solid and ribbed slab test results

4.5.1 | Punching of solid slab

The test results are compared to the punching provisions of the *fib* Model Code 2010 LoA-III.⁵⁵ The provisions are based on the critical shear crack theory (CSCT,^{56,57}). The

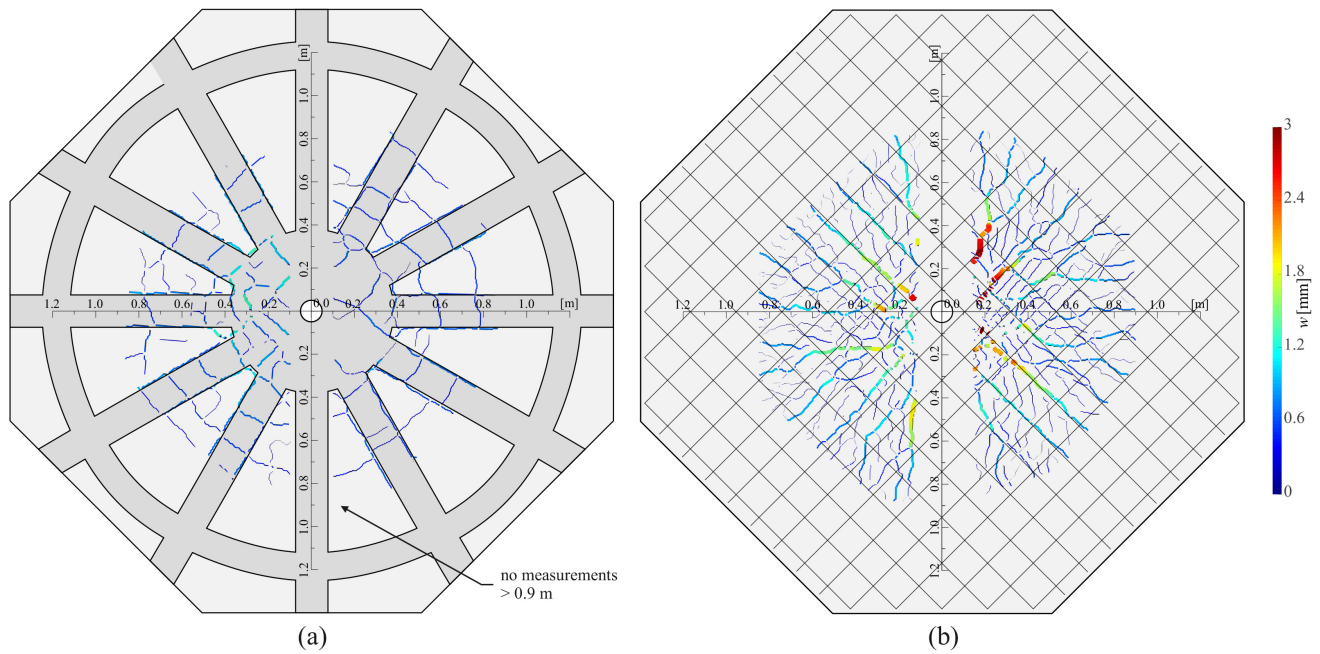


FIGURE 14 Cracking pattern at maximum load of slab tests: (a) S1: ribbed and (b) S2: solid.

fundamental assumption is the proportionality of the crack width w to the rotation of the slab ψ multiplied by the depth d .⁵⁷ The punching resistance is determined by a superposition of the concrete and steel contributions ($V_{Rd} = V_{Rd,c} + V_{Rd,s}$), both of which are dependent on the rotation ψ . Additionally, the capacity of the concrete strut must be verified. The formulas are given in Appendix C and the results are shown in Figure 12b.

The punching resistance V_{mod} and the slab rotation ψ_{mod} at ultimate load were evaluated using the mean values of material properties (Tables 3 and 4) and without safety factors, yielding very accurate predictions ($V_{exp}/V_{mod} = 702/728$ kN = 96%, $\psi_{exp}/\psi_{mod} = 0.0204/0.0201 = 1.01$ at maximum load level; see Figure 12b).

4.5.2 | Flexural failure of the ribbed slab

The distribution of bending moments in a continuous slab is commonly calculated using linear-elastic finite element analysis and assuming a linear elastic slab response (Section 2.2). Cracking allows for the redistribution of forces, and the activation of reinforcement in all directions whenever possible. As a result, linear-elastic calculations are not suitable to evaluate the bending resistance of the ribbed slab. Instead, flexural failure can be studied using the yield line method based on plasticity theory.³² Generally, an upper bound solution can be found by applying a freely chosen kinematically admissible failure mechanism. Conversely, when evaluating a test, the

failure load should be found by using the observed failure mechanism. Hence inspired by Figure 13a–c, the failure mechanism is modeled as a truncated cone (Figure 15), with a circular yield line around the solid column part and a funnel between this circle and the supports:

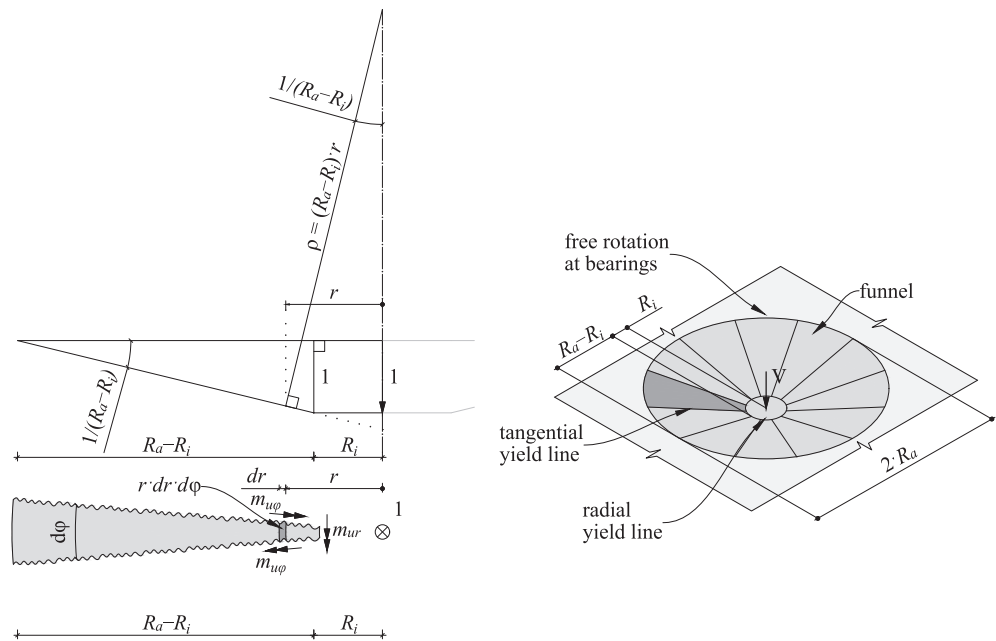
The application of the failure mechanism shown in Figure 15 yields the following resistance:

$$V \leq 2\pi \left(m_{up} + m_{ur} \cdot \frac{R_i}{R_a - R_i} \right), \quad (4)$$

where m_{ur} and m_{up} are the radial and tangential flexural strength per unit length, respectively, R_i is the radius of the solid column part and R_a is the outer radius of the funnel. The full derivation of Equation (4) is given in Appendix B.

The required flexural strength values are evaluated using INCA2⁵³ (Appendix B) assuming the respective material properties (Tables 3 and 4). The radial flexural strength $m_{ur} = 415.5$ kNm/m was calculated at the section around the solid column to rib transition ($R_i = 0.38$ m, failure location in Figure 13b). The averaged value for flexural strength in the tangential direction yields in $\bar{m}_{up} = 35.8$ kNm/m (see Appendix B, corresponding to failure crack in Figure 13b). Evaluating Equation (4) yields a failure load of 1435 kNm, which is slightly (−0.5%) below the the observed peak load of 1442 kN. Note that the effect of combining radial reinforcement in the ribs and orthogonal reinforcement with supplementary reinforcement in the slab was neglected.

FIGURE 15 Evaluation of the test results with the concept of yield lines.



5 | SUMMARY AND CONCLUSIONS

This paper investigates the potential of automated formwork construction for material-efficient RC slabs. Pertinent structural design requirements are discussed and introduced in a digital design-to-production workflow for ribbed RC slabs with 3D-printed formwork. The material savings potential achieved by planning with this workflow and using optimization loops was demonstrated in a case study of an 8×8 m point-supported slab for office buildings comparing the concrete consumption to that of an equivalent solid slab. Furthermore, full-scale parts of the case study—a column section and three ribs with different layouts—were produced using 3D printed formwork. These elements were tested until failure to investigate their load-bearing behavior. Based on this investigation, the following conclusions can be drawn:

- The introduced production workflow demonstrates the feasibility of integrating several steps of the structural design, a task carried out by structural engineers, in the Grasshopper environment, which is a tool that is available to designers. This is regarded as an essential step in developing holistic workflows for the digital design of esthetically appealing and code-compliant structures.
- In typical office buildings, ribbed slabs provide a material savings potential of 40% when compared to structurally equivalent solid slabs. The optimum solution can be found through size optimization by introducing

a loop aiming for the lowest material consumption while ensuring compliance with long-term deflection criteria.

- Using fused deposition modeling of polymers as formwork is a suitable method for producing large-scale customized structural elements integrating conventional steel reinforcement. The structural tests confirmed the structural integrity of the resulting components, and established design principles could reliably describe their load-bearing behavior. The longitudinal reinforcement could be fully activated in all cases, ensuring the desired ductile failure modes.
- Automated formwork technologies allow for the creation of smooth transitions between different parts of a structure based on the anticipated force-flow, which is a key advantage to producing structurally efficient structures, as confirmed by the structural test of the slab-to-column demonstrator, where in contrast to the solid slab, punching was avoided.
- The comparison of a section of the optimized ribbed slab around the column with an equivalent solid slab shows a much stiffer load-bearing behavior and almost double bearing capacity. This demonstrates the potential of placing the material where it is structurally required.
- In addition to the challenges involved in the production and placement of curved reinforcement, the structural effects of curved ribs should be considered, because the associated secondary effects may influence the overall structural capacity. To this end, this paper presents and validates a concept for avoiding cracking due to deviation forces caused by curved reinforcing bars in the tension chord of the ribs.

NOMENCLATURE

A_s	cross-sectional area of the bottom longitudinal reinforcement
$A_{s'}$	cross-sectional area of the top longitudinal reinforcement
D_{\max}	maximum aggregate size
E_s	Young's modulus of the longitudinal reinforcing bars
F	force; point load
L	span
M	bending moment
V	shear force
a	distance of the reinforcing bar axis to the surface of the concrete
a_{sw}	cross-sectional area of the shear reinforcement per unit length
b	width
d	static depth
e	lever arm
f_c	concrete cylinder compressive strength
f_{ct}	tensile strength of the concrete
f_{su}	tensile strength of the reinforcement
f_{sy}	yield strength of the reinforcement
h	height
h_s	height of the slab
m	mean value
m_c	mass of concrete
m_{ur}	radial flexural strength
$m_{u\varphi}$	tangential flexural strength
q	uniformly distributed load
r	radius
s	spacing of the ribs
w	deflection
δ	relative deflection
ε_{sy}	reinforcement strain at yielding
ε_{su}	total elongation of the reinforcement at maximum force in a tension test
ρ_s	reinforcement ratio
ρ_w	shear reinforcement ratio
σ	stress
φ	creep coefficient
ψ	rotation
3DCP	three-dimensional concrete printing
ACDM	automated crack detection and measurement
CoV	coefficient of variation
CFRP	carbon-fiber-reinforced polymers
CNC	computer-numerical-controlled
DIC	digital image correlation
EC2	EN1992-1-1, EN1992-1-2

EPS	expanded polystyrene
FE	finite element
FEA	finite element analysis
FRC	fiber-reinforced concrete
FDM	fused deposition modeling
GH	Grasshopper
BJ	binder jetting
MC10	<i>fib</i> Model Code 2010
NC	normal concrete
OSB	oriented strand board
PLA	polylactic acid
RC	reinforced concrete
RFEM	Dlubal RFEM
SCC	self-compacting concrete
SLS	serviceability limit state
ULS	ultimate limit state
UHPFRC	ultra-high-performance fiber-reinforced concrete
VIC	software for DIC evaluation from Correlated Solutions
\emptyset	diameter

AUTHOR CONTRIBUTIONS

Conceptualization, methodology, writing—original draft preparation: Tobias Huber; review and editing: Jaime Mata-Falcón, Walter Kaufmann, Tobias Huber; experimental work, specimen production, project administration: Tobias Huber, Joris Burger; funding acquisition: Jaime Mata-Falcón; supervision: Jaime Mata-Falcón, Walter Kaufmann. The manuscript's published version has been read and approved by all authors.

ACKNOWLEDGMENTS

The authors thank Siemens, Geberit and the ETH Zurich Foundation for their financial support. This research was also supported by the Swiss National Science Foundation's NCCR Digital Fabrication (agreement number 51NF40-141853). Furthermore, the authors express their appreciation for the material support provided by SACAC and Debrunner Acifer, as well as the fruitful collaboration between the parties involved in this research.

FUNDING INFORMATION

Siemens, Geberit and the ETH Zurich Foundation provided funding for this project.

CONFLICT OF INTEREST STATEMENT

The authors state that they have no conflict of interest. The funders played no role in the study's design, data collection, analyses, interpretation of data, manuscript writing, or decision to publish the results.


DATA AVAILABILITY STATEMENT


The data that support the findings of this study are available from the corresponding author upon reasonable request.

ORCID

Tobias Huber  <https://orcid.org/0000-0001-9248-1662>

Joris Burger  <https://orcid.org/0000-0001-6116-8091>

Jaime Mata-Falcón  <https://orcid.org/0000-0001-8701-4410>

Walter Kaufmann  <https://orcid.org/0000-0002-8415-4896>

REFERENCES

- Hennebique F. Verfahren zur Herstellung von Decken bzw. Fußböden aus armiertem Beton. 1903;AT12365B:6.
- Gasparini DA. Contributions of C.A.P. TURNER to development of reinforced concrete flat slabs 1905–1909. *J Struct Eng*. 2002;128:128–1252.
- Fürst A, Marti P. Robert Maillart's design approach for flat slabs. *J Struct Eng*. 1997;123:1102–10. [https://doi.org/10.1061/\(ASCE\)0733-9445\(1997\)123:8\(1102\)](https://doi.org/10.1061/(ASCE)0733-9445(1997)123:8(1102))
- Halpern AB, Billington DP, Adriaenssens S. The ribbed floor slab systems of Pier Luigi Nervi n.d.:7.
- Antony F, Griebhammer R, Speck T, Speck O. Sustainability assessment of a lightweight biomimetic ceiling structure. *Bioinspir Biomim*. 2014;9:016013. <https://doi.org/10.1088/1748-3182/9/1/016013>
- 2020 Global Status Report for Buildings and Construction. Towards a zero-emission, efficient and resilient buildings and construction sector. Nairobi: United Nations Environment Programme; 2020.
- The European green deal. COM(2019) 640 final. final. Brussels: European Commission; 2019.
- Han D, Yin H, Qu M, Zhu J, Wickes A. Technical analysis and comparison of formwork-making methods for customized prefabricated buildings: 3D printing and conventional methods. *J Archit Eng*. 2020;26:04020001. [https://doi.org/10.1061/\(ASCE\)AE.1943-5568.0000397](https://doi.org/10.1061/(ASCE)AE.1943-5568.0000397)
- Jipa A, Dillenburger B. 3D printed formwork for concrete: state-of-the-art, opportunities, challenges, and applications. *3D Print Addit Manuf*. 2021;9(2):84–107. <https://doi.org/10.1089/3dp.2021.0024>
- Wangler T, Lloret E, Reiter L, Hack N, Gramazio F, Kohler M, et al. Digital concrete: opportunities and challenges. *RILEM Tech Lett*. 2016;1:67–75. <https://doi.org/10.21809/rilemtechlett.2016.16>
- Popescu M, Reiter L, Liew A, Van Mele T, Flatt RJ, Block P. Building in concrete with an ultra-lightweight knitted stay-in-place formwork: prototype of a concrete shell bridge. *Structure*. 2018;14:322–32. <https://doi.org/10.1016/j.istruc.2018.03.001>
- Mata-Falcón J, Bischof P, Huber T, Anton A, Burger J, Ranaudo F, et al. Digitally fabricated ribbed concrete floor slabs: a sustainable solution for construction. *RILEM Tech Lett*. 2022;7:68–78. <https://doi.org/10.21809/rilemtechlett.2022.161>
- Costas Georgopoulos and Andrew Minson (eds): Sustainable concrete solutions, Hoboken, NJ: Wiley-Blackwell; 2016.
- Ženišek M, Pešta J, Tipka M, Kočí V, Hájek P. Optimization of RC structures in terms of cost and environmental impact—case study. *Sustainability*. 2020;12:8532. <https://doi.org/10.3390/su12208532>
- Bischof P, Mata-Falcón J, Kaufmann W. Fostering innovative and sustainable mass-market construction using digital fabrication with concrete. *Cem Concr Res*. 2022;161:106948. <https://doi.org/10.1016/j.cemconres.2022.106948>
- Anton A, Jipa A, Reiter L, Dillenburger B. Fast complexity: additive manufacturing for prefabricated concrete slabs. In: Bos FP, Lucas SS, Wolfs RJM, Salet TAM, editors. Second RILEM Int. Conf. Concr. Digit. Fabr., Cham: Springer International Publishing; 2020. p. 1067–77. https://doi.org/10.1007/978-3-030-49916-7_102
- Meibodi MA, Jipa A, Giesecke R, Shammass D, Bernhard M, Leschok M, et al. Smart slab—computational design and digital fabrication of a lightweight concrete slab. In: Anzalone P, Del Signore M, Wit AJ, editors. Acadia 2018 Recalibration: On Imprecision and Infidelity: Proceedings of the 38th Annual Conference of the Association for Computer Aided Design in Architecture, Association for Computer Aided Design in Architecture (ACADIA); 2018. p. 434–443.
- Liew A, López DL, Van Mele T, Block P. Design, fabrication and testing of a prototype, thin-vaulted, unreinforced concrete floor. *Eng Struct*. 2017;137:323–35. <https://doi.org/10.1016/j.engstruct.2017.01.075>
- Jipa A, Barentin CC, Lydon G, Rippmann M, Chousou G, Lomaglio M, et al. 3D-printed formwork for integrated funicular concrete slabs. In: Lázaro C, Bletzinger KU, Oñate E, editors. Proc. IASS Annu. Symp. Volume 2019. Madrid: International Association for Shell and Spatial Structures (IASS); 2019. p. 1–8.
- Ranaudo F, Van Mele T, Block P. A low-carbon, funicular concrete floor system: design and engineering of the HiLo floors. Snijder B, De Pauw B, van Alphen S, Mengeot, P, editors. Proc. IABSE Congr. Ghent 2021. Volume 2021. Zurich: International Association for Bridge and Structural Engineering (IABSE); 2021. p. 2016–24. <https://doi.org/10.2749/ghent.2021.2016>
- Bedarf P, Szabo A, Zanini M, Heusi A, Dillenburger B. Robotic 3D printing of mineral foam for a lightweight composite concrete slab. In: van Ameijde J, editor. Proc. 27th Int. Conf. Assoc. Comput.-aided Archit. Des. Res. Asia CAADRIA. Volume 2. Hong Kong: Computer-Aided Architectural Design Research in Asia (CAADRIA); 2022. p. 61–70.
- Jipa A, Bernhard M, Meibodi M, Dillenburger B. 3D-printed stay-in-place formwork for topologically optimized concrete slabs. In: Bieg K, editor. Proc. 2016 TxA Emerg. Des. Technol. Conf., San Antonio; Austin: Texas Society of Architects; 2016. p. 97–107.
- Meibodi M, Bernhard M, Jipa A, Dillenburger B, Menges A, Sheil B. The smart takes from the strong: 3D printing stay-in-place formwork for concrete slab construction. In: Sheil B, Menges A, Glynn R, Skavara M, Lee E, editors. Fabricate 2017: Rethinking Design and Construction. Volume 3. London: UCL Press; 2017. p.210–8.
- Hansemann G, Schmid R, Holzinger C, Tapley JP, Kim HH, Sliskovic V, et al. Additive fabrication of concrete elements by robots. In: Burry J, Sabin JE, Sheil B, Skavara M, editors. Fabricate 2020: Making Resilient Architecture. London: UCL Press; 2020. p. 124–9.

25. Asprone D, Menna C, Bos FP, Salet TAM, Mata-Falcón J, Kaufmann W. Rethinking reinforcement for digital fabrication with concrete. *Cem Concr Res*. 2018;112:111–21. <https://doi.org/10.1016/j.cemconres.2018.05.020>
26. Kloft H, Empelmann M, Hack N, Herrmann E, Lowke D. Reinforcement strategies for 3D-concrete-printing. *Civ Eng Des*. 2020;2:131–9. <https://doi.org/10.1002/cend.202000022>
27. Gebhard L, Mata-Falcón J, Anton A, Dillenburger B, Kaufmann W. Structural behaviour of 3D printed concrete beams with various reinforcement strategies. *Eng Struct*. 2021; 240:112380. <https://doi.org/10.1016/j.engstruct.2021.112380>
28. Burger J, Lloret-Fritsch E, Scotto F, Demoulin T, Gebhard L, Mata-Falcón J, et al. Eggshell: ultra-thin three-dimensional printed formwork for concrete structures. *3D Print Addit Manuf*. 2020;7:48–59.
29. Burger J, Huber T, Lloret-Fritsch E, Mata-Falcón J, Gramazio F, Kohler M. Design and fabrication of optimised ribbed concrete floor slabs using large scale 3D printed formwork. *Autom Constr*. 2022;144:104599. <https://doi.org/10.1016/j.autcon.2022.104599>
30. Steffen P. Elastoplastische Dimensionierung von Stahlbetonplatten mittels Finiter Bemessungselemente und Linearer Optimierung; IBK Bericht; 220. Basel: Birkhäuser; 1996.
31. Hillerborg A. A plastic theory for the design of reinforced concrete slabs. In: IABSE Congr Rep. Zurich: International Association for Bridge and Structural Engineering (IABSE); 1960;6: 177–186. <https://doi.org/10.5169/SEALS-6955>
32. Johansen KW. Beregning af krydsarmerede jernbetonpladers brudmoment. Bygningsstatistiske Meddelelser. 1931;3:1–18.
33. EN 1992-1-1. Eurocode 2: design of concrete structures—part 1–1: general rules and rules for buildings. Brussels: Eur Comm Stand (CEN); 2004.
34. Marti P, Kaufmann W, Seelhofer H, Karagiannis D. Kirchhoff-love plate deformations reinterpreted. *J Eng Mech*. 2022;148: 04022026.
35. International Federation for Structural Concrete, editor. Model Code 2010: final draft. Vol 2. Lausanne: International Federation for Structural Concrete; 2012.
36. Iori T. Le plancher a nervures isostatiques de Nervi. Lausanne: Press Polytech Univ Romandes PPUR; 2012.
37. EN 1992-1-2. Eurocode 2: design of concrete structures—part 1–2: general rules-structural fire design. Brussels: Eur Comm Stand (CEN); 2004.
38. EN 1991-1-1. Eurocode 1: actions on structures—densities, self-weight, imposed loads for buildings. Brussels: Eur Comm Stand (CEN); 2002.
39. EN1990. Eurocode: basis of structural design. Brussels: Eur Comm Stand (CEN); 2002.
40. Stoiber N, Kromoser B. Topology optimization in concrete construction: a systematic review on numerical and experimental investigations. *Struct Multidiscip Optim*. 2021;64:1725–49. <https://doi.org/10.1007/s00158-021-03019-6>
41. Robert McNeel & Associates. Grasshopper 3D, 2020. URL: <https://www.grasshopper3d.com/>
42. McNeel R. Rhinoceros 5—user's guide. Barcelona: Robert McNeel & Associates; 2014.
43. Dlubal Software DE. RFEM 5—spatial models calculated according to finite element method. Tiefenbach: Dlubal Software DE; 2020.
44. Preisinger C. Linking structure and parametric geometry. *Archit Des*. 1993;83:110–3. <https://doi.org/10.1002/ad.1564>
45. Apellániz D, Zimmer C. Parametric FEM toolbox 1.4.0; 2021.
46. Rutten D. Galapagos: on the logic and limitations of generic solvers. *Archit Des*. 2013;83:132–5.
47. Mele TV, Casas G, Rust R, Lytle B, Liew A, et al. compas-dev/-compas: COMPAS 1.8.0; 2021. <https://doi.org/10.5281/zenodo.5495213>.
48. Mitropoulou I, Burger J. COMPAS_SLICER: Slicing functionality for Compas v0.5.0; 2020. <https://doi.org/10.5281/zenodo.5910846>
49. Fleischmann P, Casas G. compas-rrc/compas_rrc: COMPAS RRC v1.1.0; 2021. <https://doi.org/10.5281/zenodo.4639419>.
50. Chen W-F, Trumbauer BE. Double-punch test and tensile strength of concrete. *J Mater*. 1972;7(2):148–54.
51. Gehri N, Mata-Falcón J, Kaufmann W. Automated crack detection and measurement based on digital image correlation. *Construct Build Mater*. 2020;256:119383. <https://doi.org/10.1016/j.conbuildmat.2020.119383>
52. Gehri N, Mata-Falcón J, Kaufmann W. Refined extraction of crack characteristics in large-scale concrete experiments based on digital image correlation. *Eng Struct*. 2022;251:113486. <https://doi.org/10.1016/j.engstruct.2021.113486>
53. Pfeiffer U. Inca 2: Interactive Nonlinear Cross-Section Analysis Bilinear; v2.9.0; 2019. URL: <https://www.u-pfeiffer.de/>, accessed: 24.02.2023.
54. Einpaul J, Ospina CE, Fernández Ruiz M, Muttoni A. Punching shear capacity of continuous slabs. *ACI Struct J*. 2016;113: 113. <https://doi.org/10.14359/51688758>
55. Muttoni A, Fernández RM. The levels-of-approximation approach in MC 2010: application to punching shear provisions. *Struct Concr*. 2012;13:32–41. <https://doi.org/10.1002/suco.201100032>
56. Muttoni A, Fernández RM. Shear strength of members without transverse reinforcement as function of critical shear crack width. *ACI Struct J*. 2008;105:105. <https://doi.org/10.14359/19731>
57. Fernández Ruiz M, Muttoni A. Applications of critical shear crack theory to punching of reinforced concrete slabs with transverse reinforcement. *ACI Struct J*. 2009;106:485–494. <https://doi.org/10.14359/56614>

How to cite this article: Huber T, Burger J, Mata-Falcón J, Kaufmann W. Structural design and testing of material optimized ribbed RC slabs with 3D printed formwork. *Structural Concrete*. 2023;24(2): 1932–55. <https://doi.org/10.1002/suco.202200633>

APPENDIX A: DESCRIPTION OF DIGITAL DESIGN-TO-PRODUCTION WORKFLOW

1. RFEM: calculate the directions of a solid slab's principal bending moments

2. GH: Nervi's workflow⁴ to obtain a rib layout based on the principal bending moments directions (further described in²⁹)
3. GH: choose the number of ribs (n_1, n_2) and determine a layout with equally spaced ribs (s_1, s_2)
 - (a) Set slab height h_s : $\max\{\text{fire regulations, deflections: } s_1/30 + c_{\text{nom}}\}$
 - (b) Set secondary rib width b_2 $\max\{\text{fire regulations, cross-section } h_2/b_2 < 3.0; \text{deviation forces}\}$
4. GH: parametric generation of structural elements (surfaces) for FEM-analysis

B + G Toolbox as an interface between GH and RFEM: translation of parametrized geometry into a finite element model, for example, structural elements, loading conditions, loads.

5. RFEM: calculate deflections w and concrete mass m_c
 6. Galapagos: parametric optimization loop minimizing concrete consumption ($m_{c,\text{min}}$), considering a specific limit for deflections (e.g., $w_{\text{max}} \leq l/300$ under quasi-permanent loads). The rib height h_1 is used as the only optimization variable, while it also influences the rib width b_1
 - (a) variation of primary rib height h_1 in midspan
 - (b) determination of the primary rib width b_1 : $\max\{\text{fire regulations; column } h_c/b_1 < 3.0; \text{cross-section deviation forces}\}$
- Steps 3–6 are repeated with different rib layouts (n_1, n_2)
7. Determine the solution with the least amount of material consumption ($m_{c,\text{min}}$)
 8. Choose a section of the slab part for formwork production
 9. Calculate the reinforcement using the equivalent frame method based on moment distribution. Verify serviceability using a linear-elastic calculation
 10. Formwork detailing, adding stiffeners²⁹
 11. Generation of print path and robotic code with extruder commands²⁹
 12. Robotic formwork fabrication²⁹

Loop back from Step 12 to Step 4 indicates the design information by printing system constraints.

APPENDIX B: RECALCULATION OF TEST RESULTS BY APPLYING THE PRINCIPLE OF YIELD LINES

B.1 | Dissipation in the funnel (tangential)

$$\text{Curvature: } \chi_1 = \rho^{-1} = \frac{1}{(R_a - R_i) \cdot r},$$

$$\text{Rotation: } \dot{\omega}_\varphi = \chi_1 \cdot r \cdot d\varphi,$$

$$\begin{aligned} \text{Dissipation energy: } dD &= m_{u\varphi} \cdot \dot{\omega}_\varphi \cdot dr \\ &= m_{u\varphi} \frac{1}{(R_a - R_i) \cdot r} dr \cdot d\varphi, \end{aligned}$$

$$D = \left\{ \int_0^{2\pi} \frac{1}{(R_a - R_i)} \int_{R_i}^{R_a} m_{u\varphi}(r, \varphi) dr \right\} d\varphi \approx 2\pi \cdot \bar{m}_{u\varphi},$$

The averaged flexural strength $\bar{m}_{u\varphi}$ per unit length was derived on the basis of Figure B1a.

$$\bar{m}_{u\varphi} = \frac{M_{u\varphi}}{R_o - R_i} = \frac{34.7}{1.35 - 0.38} = 35.8 \text{ kN/m},$$

B.2 | Dissipation in the column to rib transition (radial)

$$\text{Curvature: } \chi_1 = \frac{1}{R_a - R_i},$$

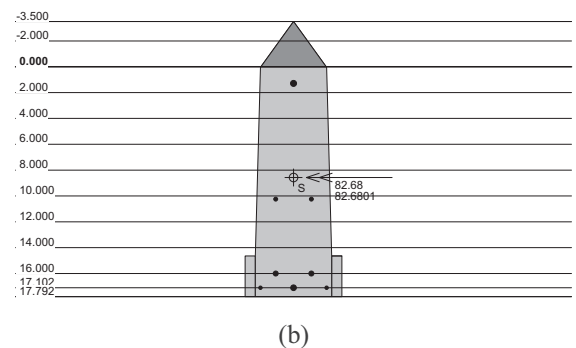
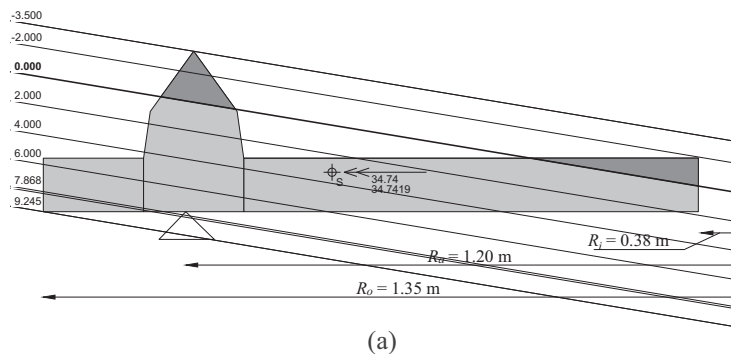


FIGURE B1 Evaluation of the flexural strength using INCA2⁵³ including a visualization of longitudinal strains: (a) $M_{u\varphi}$ in the tangential direction; and (b) M_{ur} in the radial direction.

$$\text{Rotation: } \dot{\omega}_r = \chi_1 \cdot R_i \cdot d\varphi,$$

$$\text{Dissipation energy: } dD = m_{ur} \cdot \dot{\omega}_r = m_{ur} \frac{R_i}{R_a - R_i} d\varphi,$$

$$D = \int_0^{2\pi} \frac{R_i}{R_a - R_i} m_{ur}(r, \varphi) d\varphi = 2\pi \cdot \frac{R_i}{R_a - R_i} \cdot m_{ur}.$$

The flexural strength m_{ur} per unit length was derived on the basis of Figure B1b.

$$m_{ur} = \frac{12 \cdot M_{ur}}{2 \cdot R_i \cdot \pi} = \frac{12 \cdot 82.68}{2 \cdot 0.38 \cdot \pi} = 415.5 \text{ kN/m},$$

B.3 | Application of work principles

$$W = D$$

$$V \cdot 1 = 2\pi \left(m_{u\phi} + m_{ur} \frac{R_i}{R_a - R_i} \right).$$

APPENDIX C: fib MODEL CODE 2010 PUNCHING PROVISIONS

The concrete contribution can be estimated as:

$$\begin{aligned} V_{Rd,c} &= k_{\psi} \frac{\sqrt{f_{ck}}}{\gamma_c} \cdot b_0 \cdot d_v \text{ with } k_{\psi} \\ &= \frac{1}{1.5 + 0.9 \cdot k_{dg} \cdot \psi \cdot d} \leq 0.6 \text{ and } k_{dg} \\ &= \frac{32}{16 + D_{\max}} \geq 0.75, \end{aligned} \quad (C1)$$

where d_v is the shear-resistance effective depth of the slab, d is the mean value of the flexural effective depth for the x and y directions in mm, the basic shear-resisting control perimeter b_1 is normally taken at a distance of 0.5 d_v from the supported area and D_{\max} is the maximum aggregate size in mm.

The punching reinforcement contribution is given by:

$$\begin{aligned} V_{Rd,s} &= \sum A_{sw} \cdot k_e \cdot \sigma_{swd} \text{ with } \sigma_{swd} \\ &= \frac{E_s \cdot \psi}{6} \left(1 + \frac{f_{bd}}{f_{ywd}} \cdot \frac{d}{\phi_w} \right) \leq f_{ywd}, \end{aligned} \quad (C2)$$

where for inner columns, the eccentricity factor k_e is proposed to be 0.9. If no detailed calculations are performed, the bond strength f_{bd} is assumed to be 3.0 MPa.

In the level of approximation III, the rotation of the slab ψ is defined as.

$$\psi = 1.2 \cdot \frac{r_s}{d} \cdot \frac{f_{yd}}{E_s} \cdot \left(\frac{m_{Ed}}{m_{Rd}} \right)^{1.5}, \quad (C3)$$

where the distance r_s represents the location where the radial bending moment is zero with respect to the support axis, corresponding to the point of inflection. The factor in parentheses denotes the utilized bending capacity of the support strip (width of the strip $b_s = 1.5 \cdot \sqrt{r_{sX} \cdot r_{sY}}$). If eccentricities are neglected, the average moment per unit length m_E for calculating the flexural reinforcement in the support strip could be calculated by $V/8$.

AUTHOR BIOGRAPHIES



Tobias Huber, Institute of Structural Engineering, ETH Zurich, Stefano-Franscini-Platz 5, 8093 Zurich, Switzerland; Institute of Structural Engineering, TU Wien, Vienna, Austria; Email: tobias.huber@ibk.baug.ethz.ch



Joris Burger, Institute of Technology in Architecture, ETH Zurich, Zurich, Switzerland.



Jaime Mata-Falcón, Institute of Structural Engineering, ETH Zurich, Zurich, Switzerland.



Walter Kaufmann, Institute of Structural Engineering, ETH Zurich, Zurich, Switzerland.